Instrumentation for Positron Emission Imaging

10

Pat Zanzonico

Abstract

This chapter reviews the underlying physical principles of positron emission tomography (PET) and the design and operation of state-of-the-art PET scanners. Although now a mature technology, PET has undergone, and continues to undergo, steady advances in hardware and software and, as a result, ongoing improvements in performance and functionality. Recent noteworthy advances include improvements in detector technology and image reconstruction, implementation of time-of-flight (TOF) technology, and the introduction of PET/MRI (positron emission tomography/magnetic resonance imaging) scanners.

Keywords

PET • PET/CT • PET/MRI • Scintillation detectors • Ionization detectors • Image reconstruction

Glossary

ACD	Annihilation coincidence detection
ACF	Attenuation correction factor
ACR	American College of Radiology
APD	Avalanche photodiode
BGO	Bismuth germinate
CBM	Continuous bed motion
CdZnTe (or CZT)	Cadmium zinc telluride
CF	Calibration factor
CT	X-ray computed tomography
CZT	Cadmium zinc telluride
DCE	Dynamic contrast-enhancement
DICOM	Digital imaging and communications in medicine
DOI	Depth-of-interaction
eV	Electron volt
FBP	Filtered back-projection
FOV	Field of view
FWHM	Full-width half-maximum
GSO	Cerium-doped gadolinium orthooxysilicate
keV	Kiloelectron volt (10^3 eV)
LOR	Line of response
LSO	Cerium-doped lutetium orthooxysilicate
LYSO	Cerium-doped lutetium-yttrium oxyorthosilicate
MeV	Megaelectron volt (10^6 eV)
MFP	Mean free path
MLEM	Maximum likelihood expectation maximization
MRI	Magnetic resonance imaging
MRSI	Magnetic resonance spectroscopic imaging
NaI(Tl)	Thallium-doped sodium iodide

P. Zanzonico (✉)
Memorial Hospital Research Laboratories, Department of Medical Physics, Memorial Sloan Kettering Cancer Center, New York, NY, USA
e-mail: zanzonip@mskcc.org

H.W. Strauss et al. (eds.), *Nuclear Oncology*,
https://doi.org/10.1007/978-3-319-26236-9_37

NECR	Noise-equivalent count rate
NEMA	National Electrical Manufacturers Association
OSEM	Ordered-subset expectation maximization
PEM	Positron emission mammography
PET-MRI	Positron emission tomography/magnetic resonance imaging
PET	Positron emission tomography
PET/CT	Positron emission tomography/computed tomography
PL	Penalized likelihood
PMT	Photomultiplier tube
PSF	Point-spread function
PSPMT	Position-sensitive photomultiplier tube
RAMLA	Row-action maximization-likelihood algorithm
RF	Radiofrequency
SiPM	Silicium-based photomultiplier
SNR	Signal-to-noise ratio
SPECT	Single-photon emission computed tomography
SPECT/CT	Single-photon emission computed tomography/computed tomography
SSRB	Single-slice rebinning
SUV	Standardized uptake value
TOF	Time-of-flight

Contents

Introduction

This chapter reviews the underlying physical principles of positron emission tomography (PET) and the design and operation of state-of-the-art PET scanners. Although now a mature technology, PET has undergone, and continues to undergo, steady advances in hardware and software and, as a result, ongoing improvements in performance and functionality. Recent noteworthy advances include improvements in detector technology and image reconstruction, implementation of time-of-flight (TOF) technology, and the introduction of PET/MRI (positron emission tomography/magnetic resonance imaging scanners.

Basic Principles of Radiation Detection

Radiation detectors are generally characterized as either scintillation or ionization detectors [1–3]. The application of scintillation and ionization detectors in gamma cameras and single-photon emission tomography is discussed in ▶ Chap. 11, "Instrumentation for Single-Photon Emission Imaging". In scintillation detectors, visible light is produced as radiation excites atoms of a crystal and is converted to an electronic signal, or pulse, and amplified by a photomultiplier tube (PMT) or other photodetector. In ionization detectors, free electrons produced when radiation ionizes a stopping material are collected to produce a small electronic signal. Clinical devices based on solid-state ionization detectors are available for single-photon (i.e., non-PET) imaging but remain far less common than scintillation detector-based devices.

Scintillation detectors. In scintillation detectors (Fig. 1) [1, 2], radiation interacts with and deposits energy in a scintillator. The radiation energy thus deposited is converted to visible light, with the amount of light produced being proportional to the radiation energy deposited. Because the light is emitted isotropically, the inner surface of the light-tight crystal housing is coated with a reflective material so that light emitted toward the sides and front of the crystal is

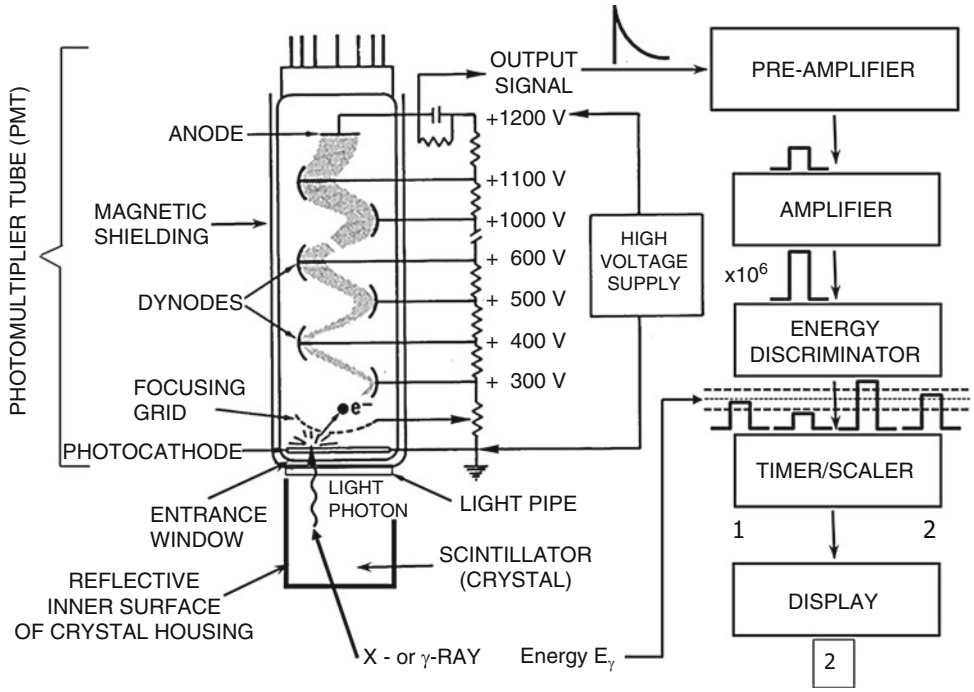

Fig. 1 Basic design and operation of a scintillation detector. Note that only two of the four pulses have heights lying between the preset pulse height ranges (indicated by the *two dash horizontal lines* below the energy discriminator, that is, corresponding to photon energies within the preset photopeak energy window) (see Fig. 1c). Thus, only those two photons are counted (in the case of a radiation counter) or included in the image (in the case of a radiation imager). The other two photons, with pulse heights and therefore energies outside the photopeak energy window, are not counted or included in the image (Adapted from references [1, 2] with permission)

reflected back toward the PMT; this maximizes the amount of light collected and therefore the overall sensitivity of the detector and ensures that the amount of light detected is proportional to the energy of the absorbed photon. Interposed between the back of the crystal and the entrance window of the PMT is the light guide, sometimes simply a thin layer of transparent optical gel. The light guide optically couples the crystal to the PMT and thus maximizes the transmission of the light signal from the crystal into the PMT.

The PMT consists of an evacuated glass enclosure, containing a series of electrodes maintained at different voltages. Coated on the inner surface of the PMT's entrance window is the photocathode. When struck by the light from the crystal, the photocathode ejects electrons. The probability that each visible light photon will eject an electron from the photocathode is 15–25%. Immediately beyond the photocathode is the focusing grid, maintained at a relatively low positive voltage relative to the photocathode. Once the "focused" electrons pass through the focusing grid, they are attracted by a relatively large positive voltage relative to the photocathode, ~300 V, on the first of a series of small metallic elements called dynodes. The resulting high-speed impact of each electron results in the ejection from the dynode surface of an average of three electrons. The electrons thus ejected are then attracted by the even larger positive voltage, ~400 V, on the second dynode. The impact of these electrons on the second dynode surface ejects an additional three electrons on average for each incident electron. Typically, a PMT has 10–12 such dynodes (or stages), each ~100 V more positive than the preceding dynode, resulting in an overall electron amplification factor of 3^{10}–3^{12} for the entire PMT. At the

collection anode, an output signal is generated. The irregularly shaped PMT output signal is shaped into a logic (i.e., square-wave) pulse that can be electronically manipulated. In the past, this was accomplished by a preamplifier; nowadays, pulse shaping, amplification, etc. are performed using solid-state electronics and computer software. The amplitudes (or "heights") of the resulting electrical pulses are proportional to the number of electrons produced at the PMT photocathode and thus the energy of the incident radiation. These pulses can then be sorted according to their respective heights by an energy discriminator (also known as a pulse height analyzer), and those pulses with a pulse height (i.e., energy) within a preset photopeak energy window are counted or included in the image. Importantly, implicit in the foregoing discussion, the amount of light produced in a scintillation detector is proportional to the radiation energy deposited in the scintillator.

In recent years, new PMT configurations have been developed that allow enhanced approaches to position determination in PET scanners. These include the position-sensitive PMT (PSPMT), which provides two-dimensional position information via two sets of wire anodes perpendicular to one another. The electrons from the last dynode stage are read out on each set of anode wires. The position of the incident light on the photocathode can then be estimated from the electron distribution on each wire. Readout of the wire anodes is typically accomplished via separate internal resistors (or functionally equivalent components) for x- and y-position information.

The silicon photodiode is an alternative to the PMT for conversion of scintillation light into electronic signals. Photodiodes typically have a gain of only 1 (compared to the ~10^6-fold gain of PMTs) and thus require low-noise electronics. The so-called avalanche photodiodes (or APDs), in which the number of electrons produced by the visible light is amplified, have considerably higher gains, of the order of 100–1,000, but still require low-noise readout electronics. An alternative to traditional vacuum-tube PMTs, Si photomultipliers (or "SiPMs"), are single-photon-sensitive devices built from a multi-pixel APD array on a Si substrate [4] and achieve essentially one-to-one correspondence between each detector element and the PMT [5]; this so-called digital SiPM design has been implemented in the Philips Vereos™ PET scanner. In the "analog" SiPM design, the signals from multiple pixels in the APD array are summed, effectively minimizing the impact of electronic noise but at the cost of additional circuitry [5]. The dimension of each single APD can vary from 20 to 100 μm and their density can be up to 1,000/mm^2. The supply voltage typically varies between 25 and 70 V, 30- to 50-fold lower than that required for traditional PMTs. Performance parameters of SiPMs are comparable to those of traditional PMTs but with a much more compact form factor.

The scintillation detection materials most widely used in Nuclear Medicine – all inorganic scintillators – are bismuth germanate (BGO, $Bi_4Ge_3O_{12}$), cerium-doped gadolinium oxyorthosilicate (GSO (Ce) or GSO, Gd_2SiO_5:Ce), cerium-doped lutetium oxyorthosilicate (LSO(Ce) or LSO, Lu_2SiO_5:Ce), and cerium-doped lutetium-yttrium oxyorthosilicate (LYSO(Ce) or LYSO, Lu_2YSiO_5:Ce) as well as thallium-doped sodium iodide (NaI(Tl)) (Table 1) [1, 2, 6, 7]. PET scanners primarily use BGO, GSO, LSO, or LYSO. The most important practical features of scintillation detectors include:

high mass density (ρ) and effective atomic number (Z_{eff}) – to maximize the photon stopping power (i.e., intrinsic efficiency ε) of the detector;
high light (scintillation) output – to maximize the signal and thus minimize statistical uncertainty in the energy of the detected signal;
for PET, speed of the output light pulse – to shorten the coincidence timing window (τ) and thus minimize the number of random events (see below) without sacrificing a significant portion of the signal.

As noted, higher-ρ and higher-Z_{eff} atomic materials such as BGO, GSO, LSO, and LYSO have emerged as the detectors of choice for PET because of their greater stopping power for 511-keV annihilation γ-rays. The mean free path (MFP) for 511-keV γ-rays is at least twice as long in NaI(Tl) than in BGO, GSO, or LSO. GSO,

Table 1 Physical properties of scintillation detector (crystal) materials [1, 2, 6, 7]

Material[a]	Composition	Density, ρ (gm/cm^3)	Effective atomic number Z_{eff}	Linear attenuation coefficient, μ, for 511 –keV γ-rays (/cm)	Relative probability of photoelectric interaction (%)	Light output (photons per MeV)	Scintillation decay time (ns)	Scintillation wavelength λ (nm)	Energy resolution at 511 keV (% FWHM)	Hygroscopic?
Bismuth germanate (BGO)	$Bi_4Ge_3O_{12}$	7.1	75	0.95 ε(2 cm) = 0.72[a]	40	9,000	300	480	16	No
Cerium-doped gadolinium oxyorthosilicate (GSO)	Gd_2SiO_5:Ce	6.7	59	0.70 ε(2 cm) = 0.57[a]	25	8,000	60	440	12	No
Cerium-doped lutetium oxyorthosilicate (LSO)	Lu_2SiO_5:Ce	7.4	66	0.88 ε(2 cm) = 0.69[a]	32	30,000	40	420	20	No
Cerium-doped lutetium-yttrium oxyorthosilicate (LYSO)	$LuYSiO_5$:Ce	7.4	66	0.87 ε(2 cm) = 0.68[a]	30	17,000	42	430	20	No
Thallium-doped sodium iodide NaI(T1)	NaI:T1	3.7	51	0.34 ε(2 cm) = 0.24[a]	17	41,000	230	410	8	Yes

Except for NaI(Tl), which is the scintillator used almost exclusively in gamma cameras, the other scintillators are used for PET

[a]The intrinsic efficiency of 2-cm thick coincidence detectors for 511-keV annihilation γ-rays

LSO, and LYSO have almost tenfold faster light output than BGO, with LSO and LYSO having a much greater (two- to threefold greater) light output than either BGO or GSO. The light output of scintillators (expressed as the number of light photons produced per MeV of radiation energy absorbed) is largely determined by quenching (i.e., the combined effect of all radiationless de-excitation processes in which the deposited energy is ultimately degraded to heat). GSO has somewhat better energy resolution, and therefore scatter rejection capability, than either BGO or LSO. A notable disadvantage of LSO and LYSO is the presence of a naturally occurring long-lived radioisotope of lutetium, lutetium-176 (^{176}Lu) [6]. ^{176}Lu has an isotopic abundance of 2.6% and a half-life of ~4×10^{10} years and emits two prompt γ-rays (88% abundance) of 201 and 306 keV in energy; their summed energy of 507 keV falls well within the 511-keV energy windows commonly used in PET scanners. For example, the presence of ^{176}Lu results in a measured background count rate of 240 cps/cm^3 of LSO. For most applications, however, this has a negligible impact on typical PET scans.

Semiconductor-based ionization detectors. Semiconductor radiation detectors represent the main alternative to scintillator detector-based imaging systems. Such detectors are so-called direct-conversion devices, a major advantage of which is that they avoid the random effects associated with scintillation production and propagation and conversion of the optical signal to an electronic signal. When an x- or γ-ray interacts in a semiconductor detector, one or more energetic electrons are created and subsequently lose energy through ionization, among other processes. The ionization creates electron-hole (e-h) pairs, where a hole is the positively charged electron vacancy in the valence band left when the electron has been raised into the conduction (i.e., mobile-electron) band. Application of a bias voltage creates an electric field that causes the two types of charge carriers to migrate in opposite directions. These moving charges induce transient currents in the detector electrodes, thereby allowing measurement of the detector's response to an incident x- or γ-ray.

Semiconductor detectors offer several potential advantages over scintillator detectors [8]. By eliminating the need for bulky PMTs, semiconductor imaging systems can be made much more compact, simplifying their mechanics in comparison to those of a conventional PMT-based imaging system (see below). More importantly, the direct conversion of energy deposited by x- or γ-rays into electron-hole pairs eliminates the light-to-electrical signal transduction step and the associated loss of signal. Further, since the energy required to create an e-h pair in most semiconductors employed as radiation detectors is sufficiently small (typically 3–5 eV), each incident photon generates a large number of charge carriers. In principle, therefore, Poisson noise is considerably less and energy resolution considerably better in semiconductor detectors than in scintillation detectors. Defects (i.e., inherent irregularities in the crystal lattice) can trap electrons produced by radiation and thus reduce the total charge collected. As a result of such incomplete charge collection due to "charge trapping," statistical uncertainty (i.e., noise) is increased and energy spectra broadened, that is, the otherwise excellent energy resolution of semiconductors is degraded. Thin semiconductors have fewer traps overall than thick detectors, but also have a lower intrinsic efficiency. Trapping can be reduced by increasing the bias voltage across the detector, but at the expense of increasing its leakage current. This results in greater electronic noise and therefore poorer overall performance. Practical, reasonably economical crystal-growing techniques have been developed for cadmium telluride (CdTe), mercuric iodide (HgI_2), and cadmium zinc telluride (CdZnTe) (also known as "CZT"), which have been incorporated into commercial intraoperative gamma probes and gamma cameras [8, 9] but not PET scanners.

PET Scanner Design

PET is based on the annihilation coincidence detection (ACD) of the two colinear (approximately 180° apart) 511-keV photons resulting from the mutual annihilation of a positron and an

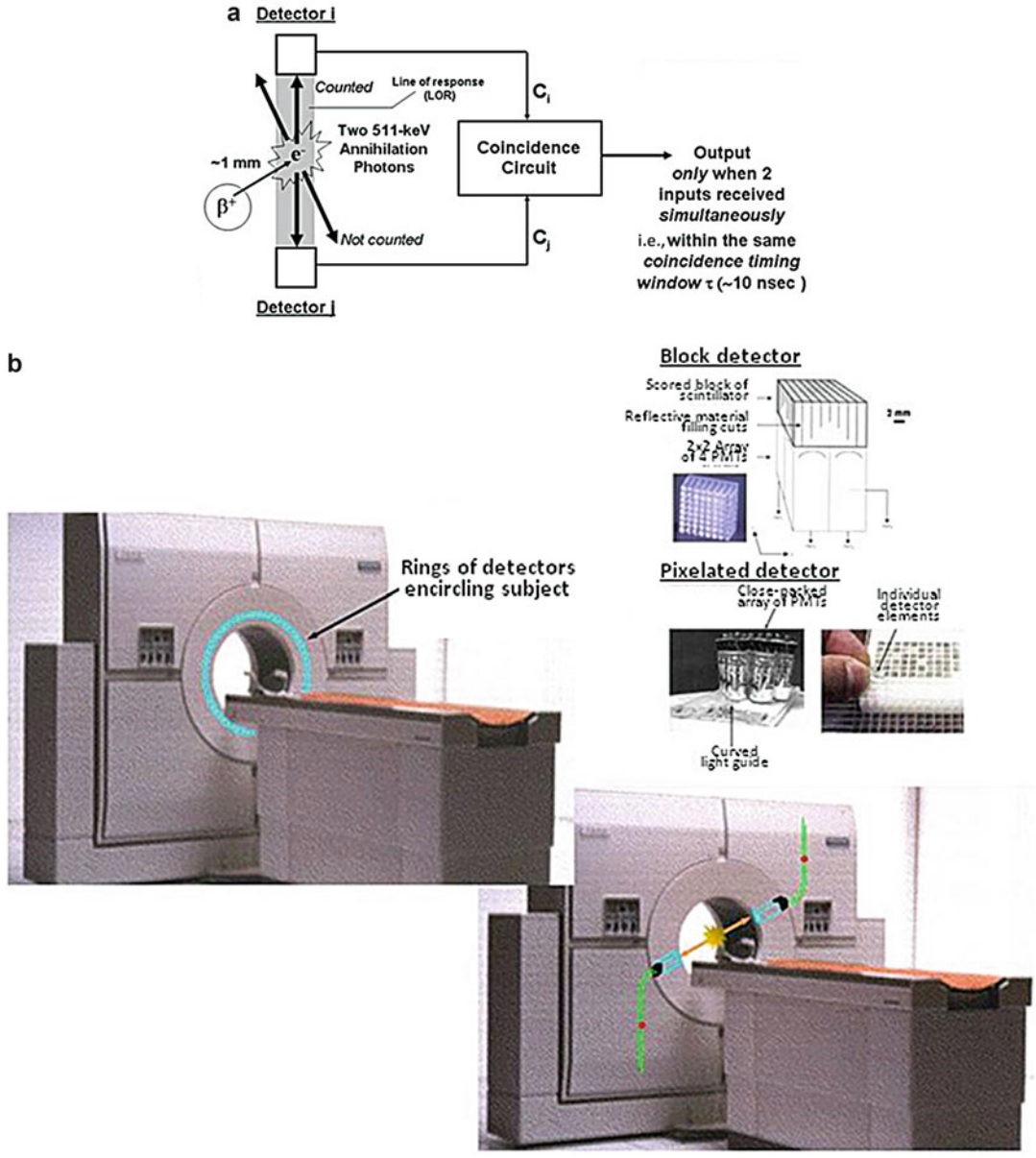

Fig. 2 **a** Annihilation coincidence detection (ACD) of the two opposed 511-keV photons resulting from positron decay and positron-electron annihilation. Note that the true coincidence (or "trues") count rate is much less than C_i and C_j. The short coincidence timing window, τ, is short (<10 ns) which minimizes the number of random coincidence events (see Fig. 8). At the same time, however, most of the annihilation photons therefore do not produce coincidence events. **b** A photograph of a PET scanner, illustrating one of a number of rings of discrete detectors encircling the subject (*left-hand panel*) and ACD of an annihilation photon by a pair of these detectors. In the insert are shown a block detector (*top*) and pixilated detectors (*bottom*) used in PET scanners. The block detector consists of a cubic piece of scintillator scored to variable depths into a two-dimensional array of detector elements, typically backed by a 2 × 2 array of PSPMTs. Pixilated detectors consist of individual scintillator detector elements backed by a continuous light guide and a close-packed array of PMTs. For both the block and pixilated detectors, the individual detector elements are typically ~2 × 2 mm in area (Adapted from reference [7] with permission)

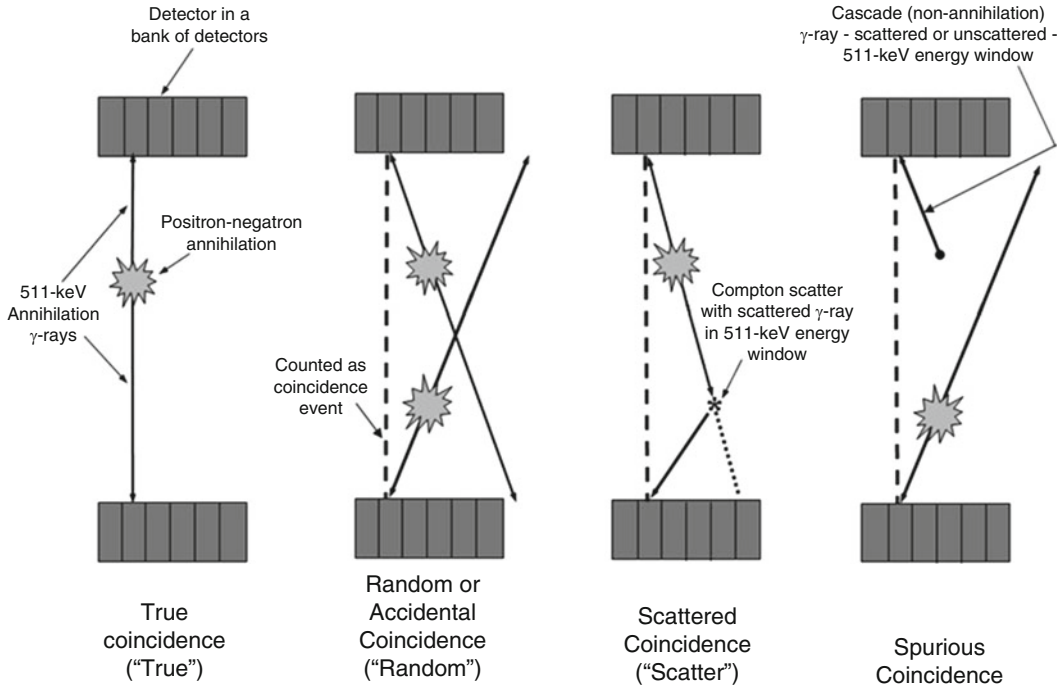

Fig. 3 The various events associated with ACD of positron-emitting radionuclides, illustrated for two opposed banks of coincidence detectors and assuming only one opposed pair of detectors, are in coincidence. A true coincidence ("true") is counted only when each of the two 511-keV annihilation photons for a single positron-electron annihilation are not scattered and are detected within the timing window τ of the two coincidence detectors. A random or accidental coincidence ("random") is an inappropriately detected and positioned coincidence (the *dashed line*) which arises from two separate annihilations, with one γ-ray from each of the two annihilations detected within the timing window τ of the coincidence-detector pair. A scattered coincidence ("scatter") is a mispositioned coincidence (the *dashed line*) resulting from a single annihilation, with one of the γ-rays undergoing a small-angle Compton scatter but retaining sufficient energy to fall within the 511-keV energy window. A spurious coincidence is an inappropriately detected and positioned coincidence (the *dashed line*) which arises from an annihilation and a cascade γ-ray, scattered or unscattered but having sufficient energy to fall within the 511-keV energy window. Spurious coincidences occur only for radionuclides which emit both positrons and high-energy prompt cascade γ-rays, that is, γ-rays with an energies (either scattered or unscattered) lying within the 511-keV energy window (From reference [7] with permission)

electron (Fig. 2a) [1, 2, 7]; a typical PET scanner and the detector configurations used in modern scanners are shown in Fig. 2b. Each individual annihilation photon is referred to as a "single" event, and the total count rate of individual annihilation photons is called the "singles count rate." When both photons from an annihilation are detected simultaneously (in coincidence), this triggers the coincidence circuit, and a "true coincidence event" ("true") is generated. The various events associated with ACD of positron-emitting radionuclides, including trues, randoms, scatter, and spurious coincidences, are illustrated in Fig. 3 [7].

The volume between the opposed coincidence detectors absorbing the two annihilation photons (the shaded area in Fig. 4) is referred to as a "line of response (LOR)" even though it is actually a volume of response. In PET, LORs are defined electronically, and an important advantage of ACD is that absorptive collimation (as is used in gamma cameras) is not required. As a result, the sensitivity of PET is two to three orders of magnitude higher than that of SPECT. Modern PET scanners generally employ a series of rings of discrete, small-area detectors (i.e., scored block detectors or pixilated detectors) encircling the subject (Fig. 2b) and, in clinical PET scanners,

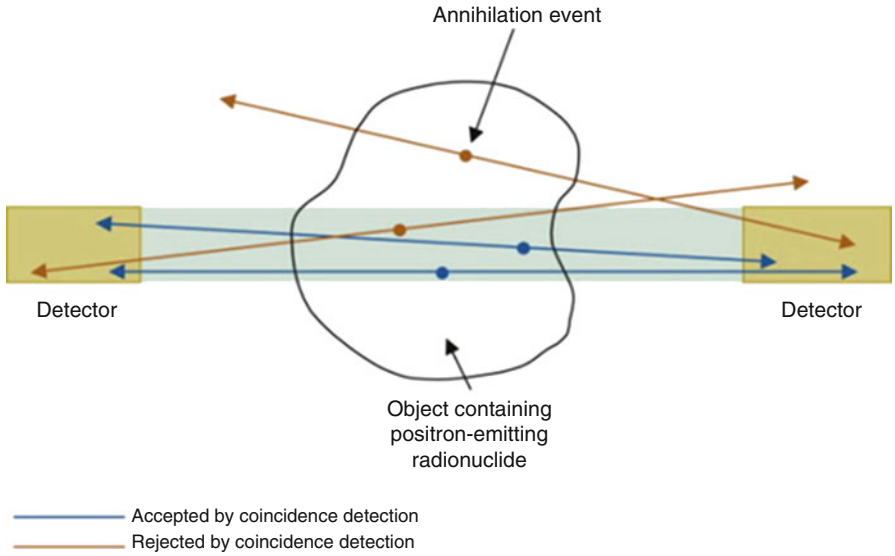

Fig. 4 For PET and annihilation coincidence detection, the 3D "line" (actually, volume) of response corresponds to the elongated cube whose cross-sectional area is defined by that of the opposed detector elements (Adapted from reference [29] with permission)

typically spanning a distance (or axial field of view (FOV)) of 15–20 cm in the patient's longitudinal direction. Recently, however, at least one PET scanner (the General Electric Discovery IQ™ scanner) with an axial FOV up to 26 cm has been marketed. Thus, a whole-body PET scan will typically require data acquisition at six to seven discrete bed positions and subsequently merge, or "knit," the discrete images into a single whole-body image. Of course, scanners with longer axial FOVs require fewer bed positions but require more detectors and front-end electronics. As its name implies, the Siemens continuous bed motion (CBM) feature allows whole-body scanning with continuous motion of the patient bed, analogous to the bed motion in spiral CT.

PET ring scanners originally employed lead or tungsten walls, or septa, positioned between and extending radially inward from the detector blocks [7] (Fig. 5). In this approach, known as two-dimensional (2D) PET, these inter-ring annular septa define plane-by-plane LORs and largely eliminate out-of-plane annihilation photons. By eliminating most of the contribution from out-of-plane randoms and scatter, image quality is improved, especially for large-volume sources (i.e., as in whole-body PET). However, 2D PET also eliminates most of the trues as well and thus reduces sensitivity. Removing the septa altogether and including coincidence events from all of the LORs among all the detectors significantly increase PET detector sensitivity. This is known as three-dimensional (3D) PET and is the prevailing design among state-of-the-art PET scanners [7, 10]. Sensitivity is increased up to ~fivefold in 3D relative to 2D PET – but with a considerable increase in the randoms and scatter count rates. Clinically, the scatter-to-true count rate ratios range from 0.2 (2D) to 0.5 (3D) in the brain and from 0.4 (2D) to 2 (3D) in the whole body [11].

A notable refinement in PET detectors has been the use of adjacent layers of two different materials with significantly different scintillation decay times (such as LSO and GSO, with decay times of approximately 40 and 60 ns, respectively); these are known as phoswich detectors [11]. Based on the pulse shape of the scintillation signal, the depth of the interaction of the annihilation photon in the detector can therefore be localized in the upper or lower layer [12]. As a result, the resolution-degrading depth-of-interaction (DOI) effect (see below) is

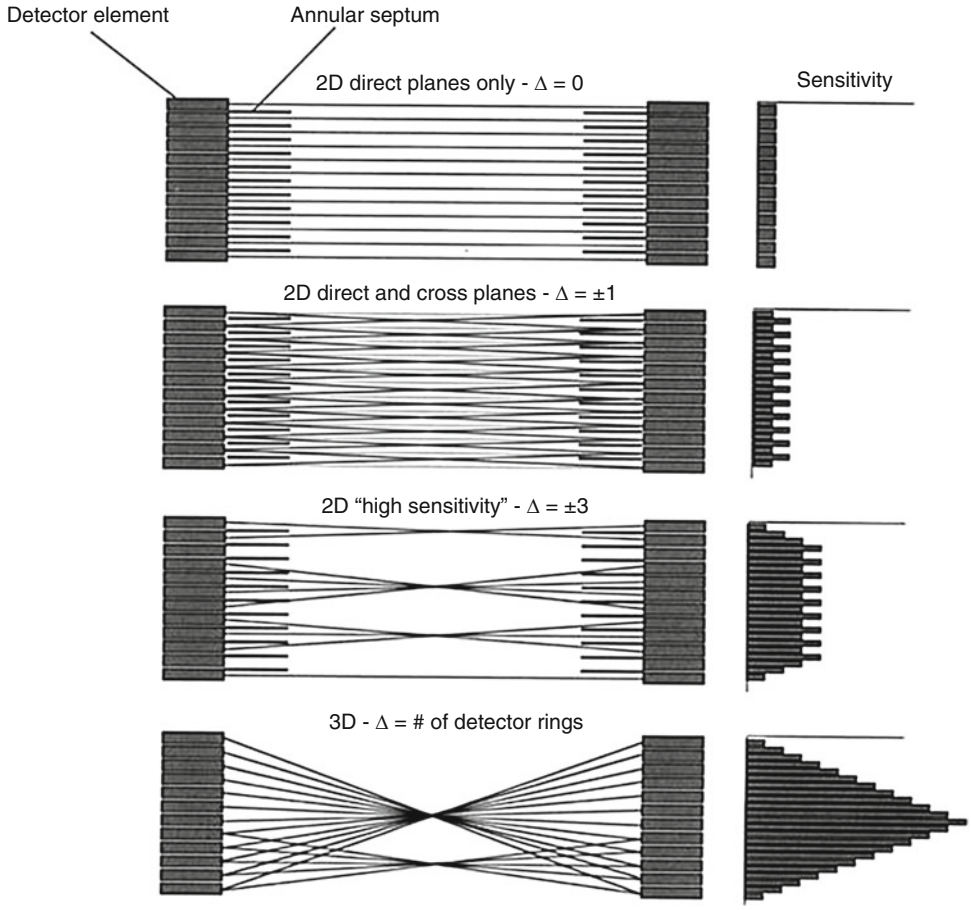

Fig. 5 Two-dimensional (2D) and three-dimensional (3D) PET data acquisition schemes (axial cross-sectional views of a multi-ring scanner) and the corresponding axial sensitivity profiles. **a**–**c** 2D data acquisition with a ring difference Δ of 0, 1, and 3, respectively. The ring difference refers to the number of different detector-element rings between which coincidence events are allowed. A ring difference of Δ of 0, for example, indicates that only intra-detector ring (i.e., direct planes) coincidences are allowed. **d** 3D (septa-less) data acquisition. The sensitivity profiles show the nonuniformity of response as a function of position along the axial FOV (Adapted from reference [11] with permission)

reduced. However, the fabrication of phoswich detectors is more complex than that of single-component detectors, and to date it has seen only limited use in commercial PET scanners, specifically preclinical scanners.

Increasingly important, time-of-flight (TOF) PET scanners utilize the measured difference between the detection times of the two annihilation photons arising from the decay of a positron (Fig. 6). This allows at least approximate spatial localization (to within ~10 cm) of the annihilation event along the LOR with current values, ~500 psec, of coincidence time resolution [13, 14]. This does not improve the spatial resolution of state-of-the-art PET scanners (~5 mm), but reduces the random coincidence rate and thus improves the signal-to-noise ratio (SNR), especially for large subjects [15]. This is important, as conventional (i.e., non-TOF) PET image quality is degraded with increasing patient size due to more pronounced attenuation and scatter and fewer trues. The use of faster digital SiPMs should improve the performance of TOF PET scanners.

The overall spatial resolution of PET scanners results from a combination of physical and instrumentation factors. There are several important

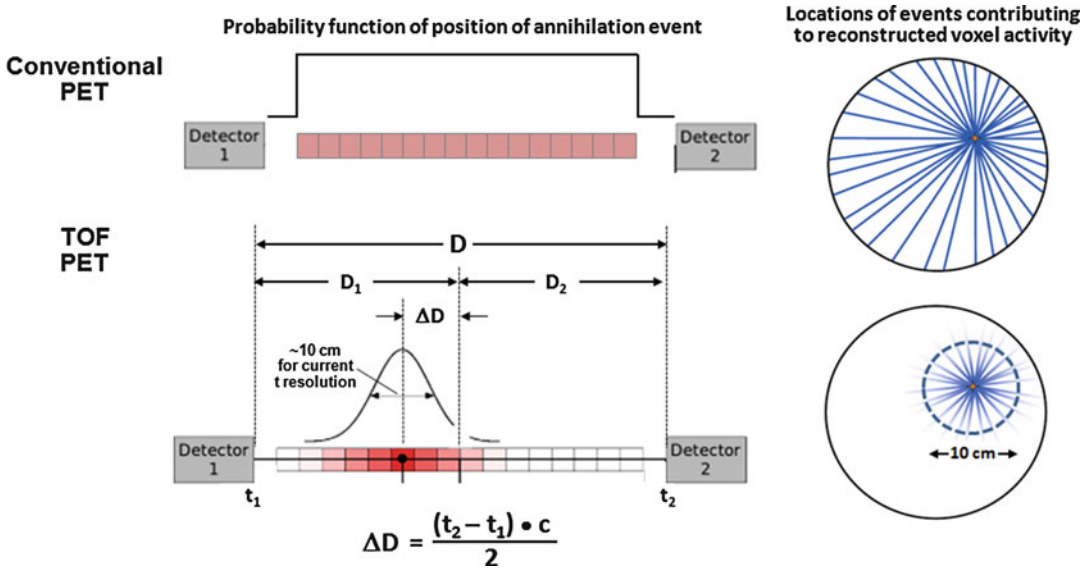

Fig. 6 Time-of-flight (TOF) PET. In conventional (i.e., non-TOF) PET, the position of a detected annihilation event may be anywhere along the LOR between the coincidence detectors. In TOF PET, the most likely position of the coincidence event along the LOR is a distance ΔD from the midpoint of the two coincidence detectors, where ΔD is proportional to the difference, $t_2 - t_1$, in times of arrival of the two annihilation photons at the two detectors (t_2 and t_1, respectively) and the speed of light, (**c**). As shown in the right panel, by localizing the position of the annihilation event, even approximately, the contribution of scatter, randoms, etc. to the reconstructed counts in each image voxel is reduced, and the SNR therefore improves. The shorter the coincidence time resolution, the more precisely the distance ΔD and the position of the coincidence event can be determined and the greater the improvement in the SNR

limitations imposed on resolution by the basic physics of positron-electron annihilation. First, for a given radionuclide, positrons are emitted over a spectrum of initial kinetic energies ranging from 0 to a characteristic maximum, or end point, energy, $E_{\max}$; the associated average positron energy, $\bar{E}$, is approximately one-third of its end point energy, $\bar{E} \approx \frac{1}{3} E_{\max}$. As a result, emitted positrons will travel a finite distance from the decaying nucleus ranging from 0 to a maximum called the extrapolated range, R_e, corresponding to its highest-energy positrons (Fig. 7a) [16]. For positron emitters used to date in PET (Table 2), the maximum energies ($E_{\max}$) vary from 0.58 to 3.7 MeV, the extrapolated ranges (R_e) from 2 to 20 mm, and the root-mean-square (rms) ranges (R_{rms}) from 0.2 to 3.3 mm. Although the finite positron range acts to blur PET images (i.e., degrade spatial resolution), the range-related blurring is mitigated by the spectral distribution of positron energies for a given radioisotope as well as the characteristically tortuous path positrons travel [16, 17]; these effects are reflected by the fact the rms positron ranges are much shorter than the extrapolated positron ranges (Table 2). The radial distance the positron travels is thus considerably shorter than its actual path length. The overall effect of positron range on PET spatial resolution, $FWHM_{\mathrm{range}}$, is illustrated quantitatively in Fig. 7b [16]. The positron range degrades spatial resolution by only ~0.1 mm for ^{18}F (E_{max} = 0.640 MeV) and ~0.5 mm for ^{15}O (E_{max} = 1.72 MeV) [16]; these values are much shorter than the respective extrapolated positron ranges.

The second physics-related limitation on PET performance is the non-colinearity of the two annihilation photons: because a positron typically has some small residual (nonzero) momentum and kinetic energy at the end of its range, the two annihilation photons are not always emitted exactly back to back (i.e., 180° apart) but deviate from colinearity by an average of 0.25° [18]. The non-colinearity-related blurring, $FWHM_{180°}$, varies from

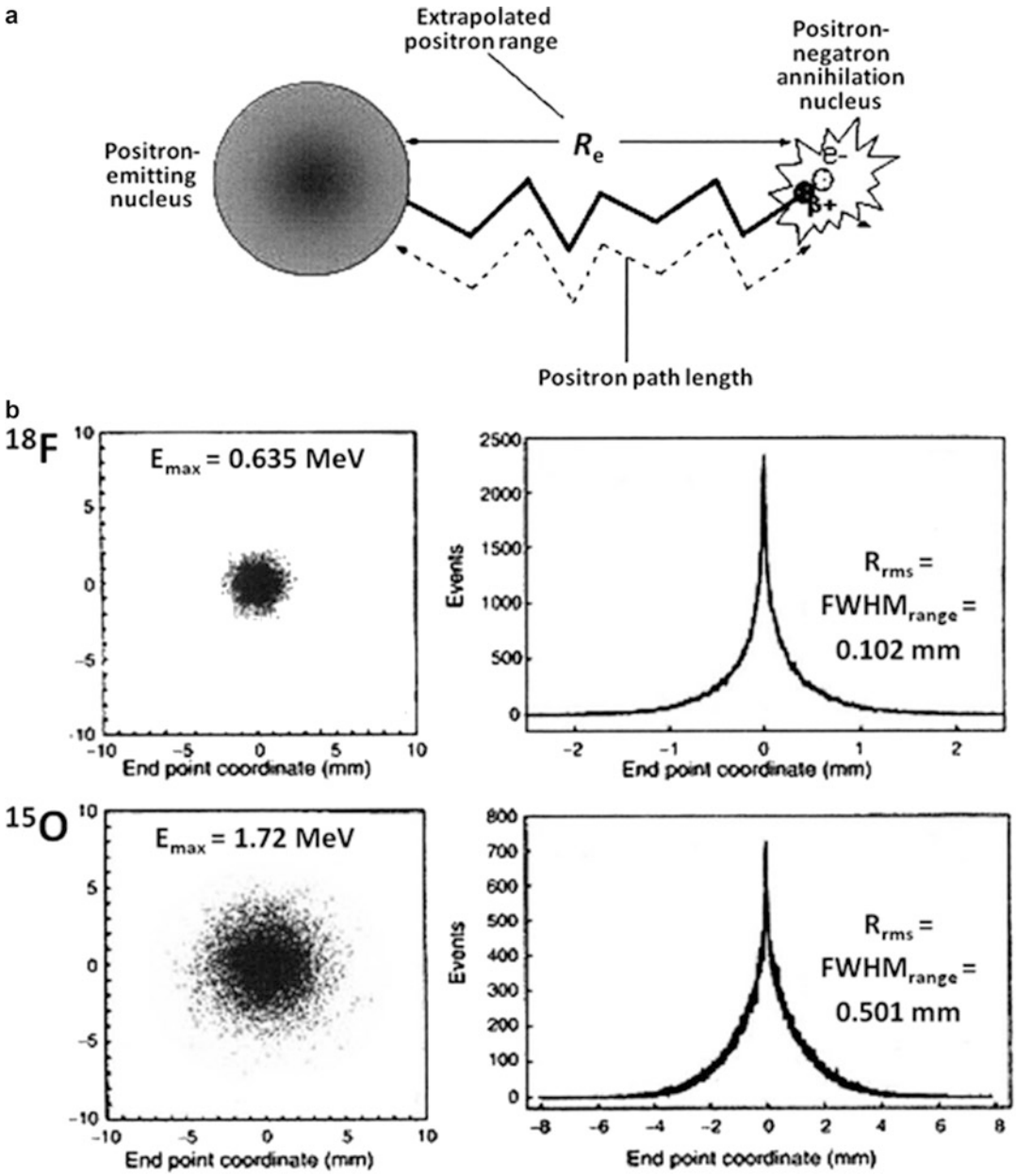

Fig. 7 Effect of positron range on PET spatial resolution. **a** Positrons travel a finite distance before undergoing annihilation, resulting in blurring of PET images. **b** The spatial dispersion of positron-electron annihilations for ^{18}F (E_{max} = 0.640 MeV) and ^{18}O (E_{max} = 1.72 MeV) as determined by Monte Carlo simulation. The annihilations for the higher-energy ^{18}O positrons are clearly more widely dispersed than those for the lower-energy ^{18}F positrons (*left panel*). A graphical representation of the resulting range-related blurring in PET, $FWHM_{range} = R_{rms}$: 1.03 mm and 4.14 mm for ^{18}F and ^{18}O, respectively (Reproduced from reference [16] with permission)

~2 mm for a 90-cm-diameter whole-body PET to ~0.7 mm for a 30-cm-diameter brain PET to ~0.3 mm for a 12-cm-diameter small-animal PET (Fig. 8) [11].

Among instrumentation-related determinants of overall spatial resolution are the intrinsic detector resolution and the depth-of-interaction effect. For discrete detector elements, the intrinsic

Table 2 Physical properties of positron-emitting radionuclides used in PET [1, 7, 70, 71]

						X- and γ-rays >0.25 MeV		
	Physical half-life	**β⁺ Branching** ratio	Maximum **β⁺** energy	**β⁺** Range in water[a] (mm)		Energy	Abundance	
Radionuclide	$T_{1/2}$	(%)	(MeV)	R_e	R_{rms}	(MeV)	(%)	Production
Carbon-11	20.4 min	99	0.96	3.9	0.4	N/A	0	Cyclotron
Nitrogen-13	9.96 min	100	1.2	5.1	0.6	N/A	0	Cyclotron
Oxygen-15	2.05 min	100	1.7	8.0	0.9	N/A	0	Cyclotron
Fluorine-18	1.83 h	97	0.64	2.3	0.2	N/A	0	Cyclotron
Copper-62	9.74 min	98	2.9	15	1.6	0.876-1.17	0.5	Generator (Zinc-62)
Copper-64	12.7 h	19	0.58	2.0	0.2	N/A	0	Cyclotron
Gallium-66	9.49 h	56	3.8	20	3.3	0.834-4.81	73	Cyclotron
Gallium-68	1.14 h	88	1.9	9.0	1.2	1.08 1.88	3.1	Generator (Germanium-68)
Bromine-76	16.1 h	54	3.7	19	3.2	0.473-3.60	146	Cyclotron
Rubidium-82	1.3 min	95%	3.4	18	2.6	0.777	13	Generator (Strontium-82)
Yttrium-86	14.7 h	32	1.4	6.0	0.7	0.440-1,920	240	Cyclotron
Zirconium-89	78.4 h	23	0.90	3.8	0.4	0.909 1.62-1.75	99 10	Cyclotron
Iodine-124	4.18 day	22	1.5	7.0	0.8	0.603-1.69	23	Cyclotron

[a] R_e is the maximum extrapolated range and R_{rms} the root-mean-square (i.e., mean) range of the β^+ particle in water and other soft tissue-equivalent media

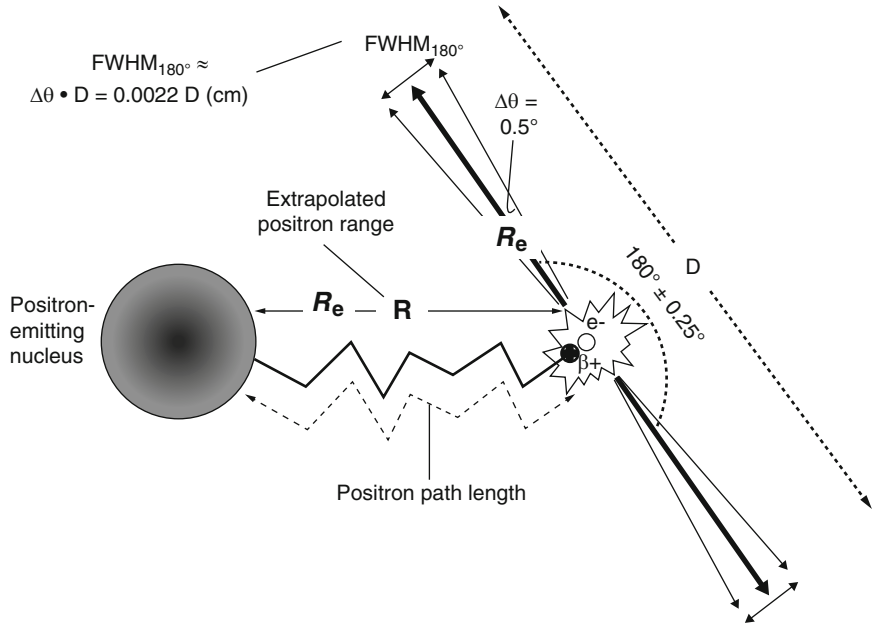

Fig. 8 Effects of the non-colinearity of the annihilation photons on PET spatial resolution. The 511-keV annihilation photons resulting from positron-electron annihilation are not always exactly colinear but may be emitted $180° \pm 0.25°$ apart [18]. The non-colinearity-related blurring, $FWHM_{180°}$, may be calculated geometrically and depends on the separation, D, of the coincidence detectors (Adapted from reference [11] with permission)

resolution, $FWHM_{\text{intrinsic}}$, is determined by the detector element width (d), increasing from $\frac{d}{2}$ midway between opposed coincidence detectors to d at the face of either detector [11].

For PET systems employing rings of discrete, small-area detectors, the depth (x) of the detector elements (2–3 cm) results in a degradation of spatial resolution termed the depth-of-interaction (DOI), or parallax, effect [11]. As illustrated in Fig. 9, with increasing radial offset of a source from the center of a detector ring, the effective detector width (d') and, with it, the intrinsic resolution, $FWHM_{\text{intrinsic}}$, increases [11]:

$$d' = d \cos\theta + x \sin\theta \tag{1}$$

and, along chords of the ring,

$$FWHM_{\text{intrinsic}} = \frac{d'}{2} \tag{2a}$$

$$= \frac{d}{2}\left(\cos\theta + \frac{x}{2}\sin\theta\right) \tag{2b}$$

where θ is the angular position of the coincident detector pair, d is the detector element width, and x is the detector element depth. In whole-body PET scanners, the detector depth (x) is typically 2–3 cm (20–30 mm), the detector width (d) about 4 mm, and the detector ring diameter about 80 cm (800 mm), and the DOI effect thus degrades spatial resolution by up to 50% at 10 cm from the center of the detector ring. Because the DOI effect decreases as the detector ring diameter increases (Fig. 9), clinical PET systems have detector rings substantially larger in diameter than that needed to accommodate patients. A variety of approaches have been developed to correct for the DOI effect in small-diameter, preclinical PET scanners, where the DOI effect is pronounced [11, 12, 19].

The spatial resolution at the center of the FOV (where the DOI effect is negligible) of a PET system, $FWHM_{\text{system}}$, can be obtained by combining the resolution of the respective components of the system:

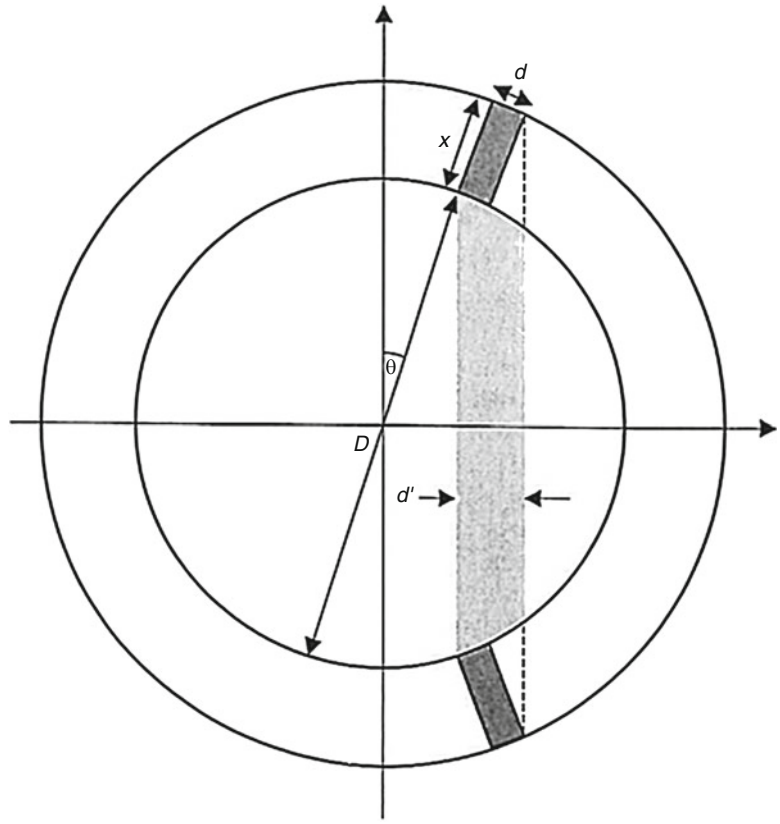

Fig. 9 The depth-of-interaction (DOI) effect. In PET scanners, the apparent width of a detector element, d′, increases with increasing radial offset from the center of the scanner. Because the depths with the detector elements at which the annihilation γ-rays interact are unknown, the apparent detector element width and therefore the effective line of response (i.e., the shaded volume) are wider than those corresponding to the actual detector element width d. The angle θ increases, and therefore the magnitude of this resolution-degrading effect, increases for sources offset further from the center of the rotation and for scanners with a smaller diameter D and a larger detector element depth x. (Reproduced from reference [11] with permission)

$$FWHM_{\text{system}} = \sqrt{FWHM_{\text{intrinsic}}{}^2 + FWHM_{\text{range}}{}^2 + FWHM_{180^\circ}{}^2} \quad (3)$$

Data "Corrections"

Even optimally performing PET scanners exhibit some nonuniformity of response [7, 20, 21]. Among the thousands of detector elements in a PET scanner, slight variations in detector thickness, light emission, optical coupling, electronic performance, etc. result in slightly different measured count rates for the same activity. In principle, such nonuniform response can be corrected by acquiring data from a uniform flux of γ-rays and normalizing to the *mean* count rate from all the LORs. This "normalization" table corrects for the nonuniform count rates among the individual LORs. One example of the effects of nonuniformity of scanner response and of the correction for nonuniform response is illustrated in Fig. 10 [20]. The normalization may be acquired using a positron-emitting rod source (e.g., germanium-68 (^{68}Ge)) spanning the entire axial FOV and rotating around the periphery of the FOV, exposing the detector pairs to a uniform photon flux per revolution. Alternatively, a uniform cylinder of a positron-emitting radionuclide can be scanned and the data thus acquired analytically corrected for attenuation; for a well-defined geometry such as a uniform cylindrical source, this correction is straightforward. However, for 3D PET, the contribution of and correction for scatter with such a large-volume source are nontrivial. Acquisition of the data required for uniformity correction is somewhat problematic in practice because of statistical considerations: typically, hundreds of millions (PET) of counts must be acquired to avoid possible "noise"-related artifacts in the uniformity correction table.

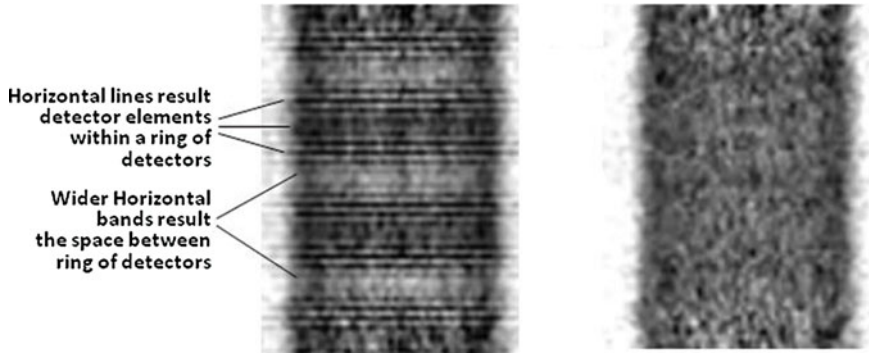

Fig. 10 Normalization (uniformity) corrections and their effects. Reconstructed PET images (coronal view) of a germanium-68 uniform-cylinder phantom without (*left panel*) and with (*right panel*) the normalization applied. The un-normalized (i.e., uncorrected) image has obvious artifacts attributable to the differences in sensitivities between direct and cross planes and the presence of separate rings of detectors. Appropriate normalization virtually eliminates these and other artifacts related to non-uniformity of the scanner response (From reference [20] with permission)

Radiation detectors are characterized by a finite "dead time" and associated count losses [11]. The dead time, typically of the order of 1–10 μsec, is the interval of time required for a counting system to record an event, during which additional events cannot be recorded. As a result, the measured count rate is systematically lower than the actual count rate. Such count losses are significant, however, only at "high" count rates (i.e., greater than ~100,000 counts per second (cps) per detector, which is of the order of the inverse of the dead time in seconds, for modern detectors). Real-time correction for dead time count losses is routinely applied in PET to the measured count rates, most commonly by scaling up the measured count rate based on an empirically derived mathematical relationship between measured and true count rates.

In PET, randoms increase the detected coincidence count rate by introducing mispositioned events and thus reduce image contrast and distort the relationship between image intensity and activity concentration [7]. One approach to random correction is the so-called delayed-window method, based on the fact that the random-coincidence photons are temporally uncorrelated (i.e., not simultaneously emitted) [22]. Briefly, once events in the coincidence timing window (typically ~10 ns or less) are detected, the number of events in a timing window equal in duration to, but much later (>50 ns later) than, the coincidence timing window is determined. More specifically, the coincidence timing window accepts events whose time difference is $\pm \tau$, while the delay window accepts events whose time difference is the delay $\pm \tau$. The number of events in the delayed timing window thus provides an estimate of the number of randoms in the coincidence timing window. Real-time subtraction of the delayed-window counts from the coincidence-window counts for each LOR thus corrects for randoms.

Another random-correction method, the "singles" method, uses the measured singles count rate for each detector and the coincidence timing window τ to calculate the random rate for each pair of coincidence detectors [23]. This approach does not require a separate measurement in a delayed-coincidence window and thus lessens the data-processing requirements on the coincidence electronics. Further, because the singles count rate is typically at least an order of magnitude higher than the coincidence-event count rate, the statistical uncertainty (noise) in the estimate of the number of randoms is much smaller than that in the number of prompt coincidences. The singles method is thus the method of choice for random correction in modern PET scanners.

Scatter results in generally diffuse background counts in reconstructed images, like randoms,

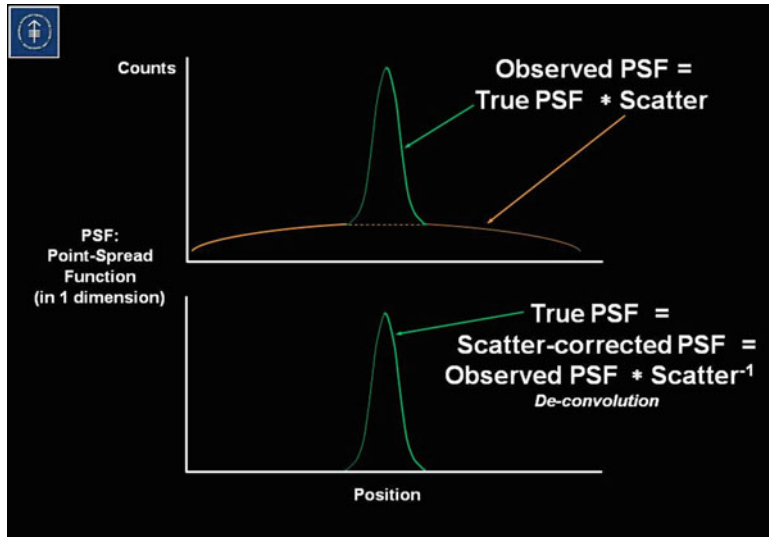

Fig. 11 The "Gaussian-fit" scatter-correction method. In practice, the point-spread function (PSF) of a PET scanner includes both primary (unscattered) and scattered counts, with the former corresponding to the Gaussian, or bell-shaped, curve and the latter corresponding to the peripheral tails extending from the Gaussian curve. The tails can be subtracted (deconvolved) from the total PSF to yield scatter-corrected PSF. In a similar manner, this scatter correction can be applied to projection images prior to reconstruction to yield scatter-corrected reconstructed images

reducing contrast and distorting the relationship between image intensity and activity concentration [24–26]. Scatter as a portion of the total PET events is far more abundant in 3D than in 2D PET (especially for body imaging of larger (i.e., adult) patients), and its correction is more challenging in 3D than in 2D PET. Perhaps the simplest scatter correction method is the "Gaussian-fit" technique [27, 28] (Fig. 11). Once the random correction has been applied, the peripheral "tails" in the projection-image count profiles, presumably due to scatter, are fit to a mathematical function and then subtracted (or deconvolved) from the measured profile to yield scatter-corrected profiles for tomographic image reconstruction. While this approach works reasonably well for 2D PET and small source volumes (e.g., the brain) in 3D PET, it is not adequate for 3D PET generally. Scatter corrections for 3D PET include dual-energy window-based approaches, convolution-/deconvolution-based approaches (analogous to the correction in 2D PET), direct estimation of scatter distribution (by computer modeling of the imaging system), and iterative reconstruction-based scatter compensation approaches (also employing computer modeling) [25, 26].

The correction for the attenuation of the photons as they pass through tissue is generally the largest correction in PET. The correction factors can range up to ~15 for a PET scan of the abdomen (equivalent to a 30-cm diameter water-equivalent cylinder). The magnitude of the correction depends on the energy of the photons (511 keV for PET studies), the thickness of tissue(s) that the photons must travel through, and the attenuation characteristics of the tissue(s). One of the attractive features of PET is the relative ease of applying accurate corrections for attenuation, based on the fact that attenuation depends only on the total thickness of the attenuation medium (at least for a uniformly attenuating medium) (Fig. 12). For a positron-emitting source and a volume of thickness L, the attenuation factor is $e^{-\mu L}$ and the attenuation correction factor $e^{\mu L}$ regardless of the position (i.e., depth) of the source. Accordingly, if a rod source of a positron emitter such as ^{68}Ge is extended along the axial FOV and rotated around the periphery of the FOV first with and then without the subject in the imaging position – the

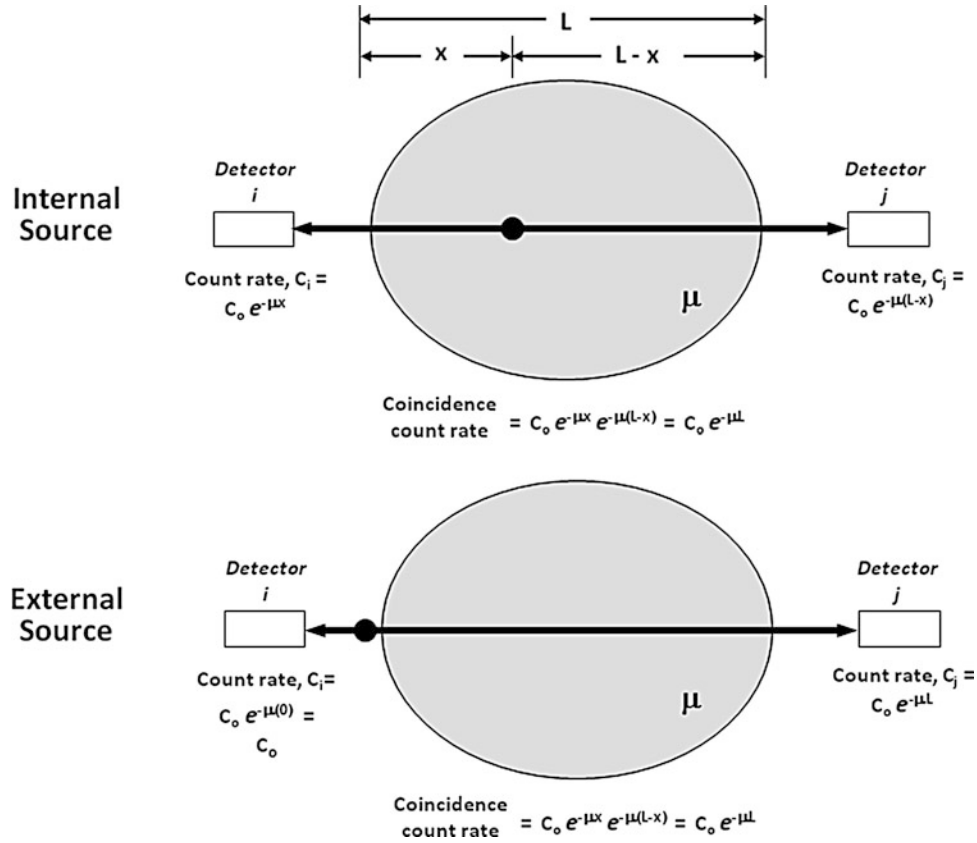

Fig. 12 In PET, attenuation of the annihilation photons for a uniformly attenuating medium depends only on the total thickness (L) of the absorber, that is, it is independent of the position (depth x) of the source in the absorber (*upper panel*). An external positron emitter can therefore be used for attenuation correction (*lower panel*). C_o is the actual source count rate, and C_i and C_j are the count rates measured by detectors i and j, respectively; μ is the linear attenuation coefficient of the absorber for 511-keV photons (Adapted from reference [7] with permission)

transmission and the blank scans, respectively – the attenuation correction factor (*ACF*) can be derived from the ratio of the counts in these respective scans:

$$ACF_{ij} = e^{\mu L}ij \tag{4}$$

$$= \frac{\left[(C)_{Blank}\right]_{ij}}{\left[(C)_{Trans}\right]_{ij}} \tag{5}$$

where ACF_{ij} is the attenuation correction factor between coincident detectors *i* and *j*, L_{ij} is the thickness of the volume between coincident detectors *i* and *j*, and $((C)_{Blank})_{ij}$ and $((C)_{Trans})_{ij}$ are the external-source counts between detectors *i* and *j* in the blank and transmission scans, respectively. In practice, a blank scan is acquired only once a day. The transmission scan can be acquired before the subject has been injected with the radiotracer, after the subject has been injected with the radiotracer but before or after the emission scan, or after the patient has been injected with the radiotracer and at the same time as the emission scan. Preinjection transmission scanning avoids any interference between the emission and transmission data but requires that the subject remain on the imaging table before, during, and after injection of the radiotracer. It is the least efficient operationally and is rarely used in practice. Postinjection transmission scanning minimizes the effects of motion, relying on the much higher external-source count rates for reliable

subtraction of the emission counts from the transmission counts. It was the most commonly used approach in "PET-only" scanners. Simultaneous emission/transmission scanning is obviously the most efficient (fastest) approach but may result in excessively high randoms and scatter counter rates in the emission data.

With the introduction of hybrid PET/CT scanners, attenuation correction is now performed using CT rather than transmission sources. A CT image is basically a two-dimensional map of attenuation coefficients at the CT X-ray energy (~80 keV). For attenuation correction of the PET emission data, however, these must be appropriately scaled to the 511-keV energy of the annihilation photons. The mass-attenuation coefficients (μ_m) for CT X-rays (~80 keV) and for 511-keV annihilation photons are 0.182 and 0.096 cm^2/gm, 0.209 and 0.093 cm^2/gm, and 0.167 and 0.087 cm^2/gm in soft tissue, bone, and lung, respectively. The corresponding μ_m ratios are therefore 1.90, 2.26, and 1.92, respectively. Thus, ACFs derived from CT images cannot be scaled to those for 511-keV annihilation photons simply using a single global factor. Accordingly, CT-based attenuation correction in PET has been implemented using a combination of segmentation (to delineate soft tissue, bone, and lung compartments) and variable scaling (to account for the different μ_m ratios in these respective tissues).

Noise-Equivalent Count Rate (NECR)

A PET scanner actually measures a so-called prompt coincidence count rate (R_{prompt}) that comprises true, scatter, and random coincidence count rates (R_{true}, $R_{scatter}$, and R_{random}, respectively):

$$R_{true} = R_{prompt} - R_{scatter} - R_{random} \qquad (6)$$

The noise-equivalent count rate (NECR) is a commonly cited performance parameter of PET scanners which accounts for the additional statistical noise introduced by the corrections for randoms and scatter (see below) [29]. It is defined as the equivalent count rate that yields the same noise level as the observed count rate after correction for randoms and scatter:

$$\mathrm{NECR} = \frac{{R_{true}}^2}{R_{true} + aR_{scatter} + bR_{random}} \qquad (7)$$

where a is the fraction of each projection that is occupied by the object being imaged and b equals 1 or 2 if the singles method or the delayed-windows method, respectively, is used for random correction. A typical plot of the NECR as function of the activity concentration is shown in Fig. 13. Because the NECR depends on the size of the object being imaged (as indicated by parameter a in Eq. 7), the plot in Fig. 13 is

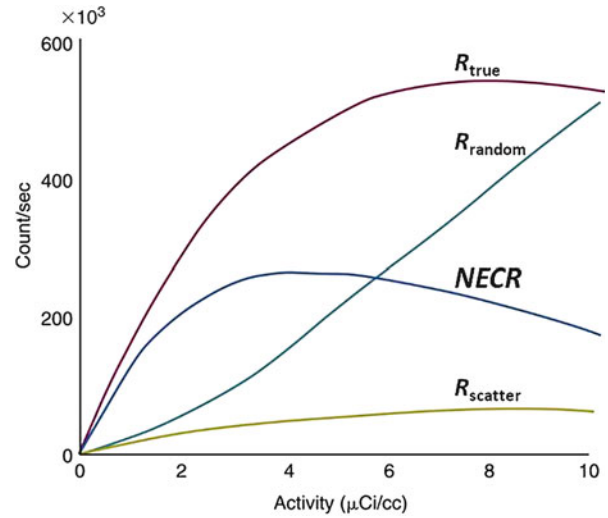

Fig. 13 The NECR and the true, scatter, and random coincidence count rates (R_{true}, $R_{scatter}$, and R_{random}, respectively) as functions of activity concentration in the fields of view for a typical clinical whole-body 3D PET scanner. The NECR indicates that the best signal-to-noise ratio is achieved at an activity concentration of ~4 μCi/cc (Adapted from reference [29] with permission)

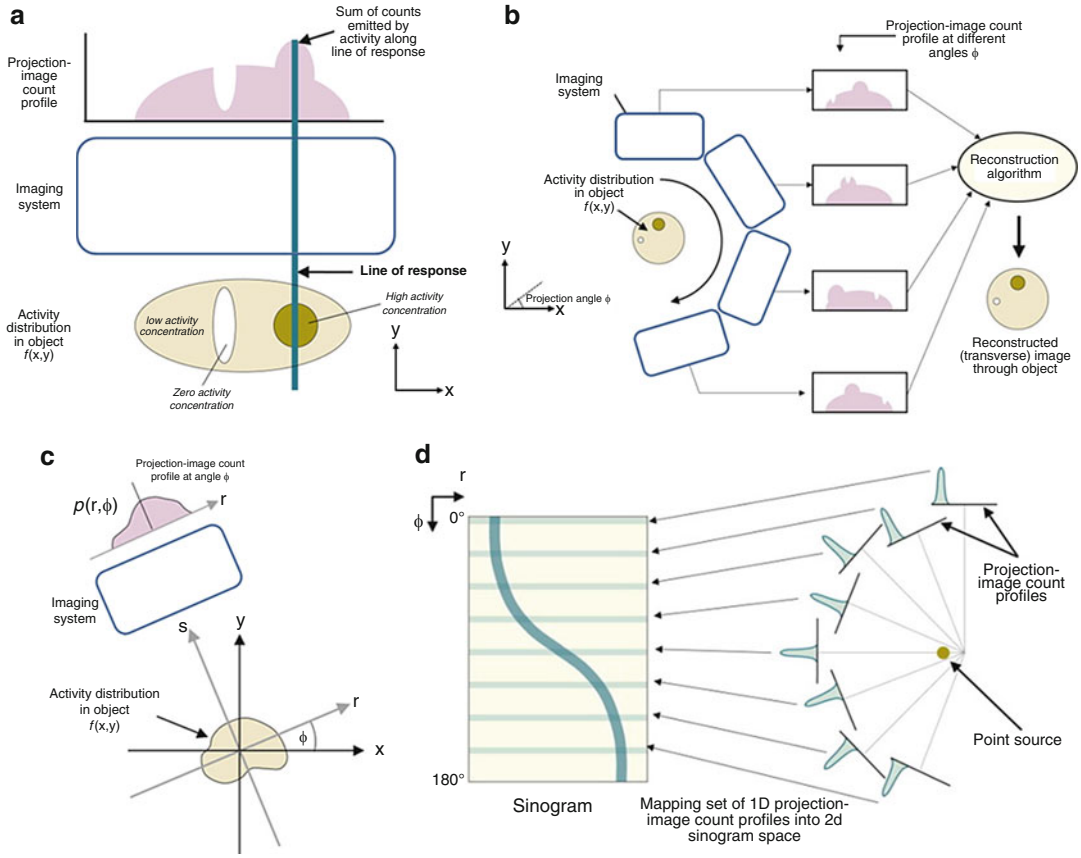

Fig. 14 Emission tomography data acquisition and sinogram display. **a** Projection-image count profile under idealized conditions (such as no attenuation or scatter). **b** Acquisition of multiple projection images and their corresponding count profiles at various projection angles ϕ about the longitudinal axis of the object being imaged. **c** The (*r*, *s*) coordinate system is rotated by projection angle ϕ with respect to the (*x*.*y*) coordinate system of the cross-section of the object being imaged. The (*r*, *s*) coordinate system is fixed with respect to the imaging system and the (*x*.*y*) coordinate system is fixed with respect to the object. **d** Two-dimensional (2D) count display, or sinogram, of a set of projection-image count profiles. Each row in the sinogram corresponds to an individual projection-image count profile, displayed for increasing projection-image angle ϕ from top to bottom. As shown, a point source of radioactivity traces out a sinusoidal path in the sinogram (Adapted from reference [29] with permission)

neither unique nor unambiguous for a particular scanner. Nonetheless, for purposes of comparison of the performance among scanners, a standard phantom can be used for derivation of the activity concentration-dependent NECR.

Image Reconstruction

In emission tomography generally, the emission data which are reconstructed to yield the tomographic images correspond to the projected sum of counts (or parallel-ray integrals) in two dimensions at various angles about the axis of the scanner (Fig. 14). In 3D PET, the projections correspond to a set of two-dimensional (x_r, y_r) integrals with azimuthal angle ϕ *and* oblique, or polar, angle θ (Fig. 15) [30]. (Correction of the emission data after the real-time dead time and random corrections and before image reconstruction – namely, normalization, scatter correction, and then attenuation correction – is typically performed in sinogram space (Fig. 14d).) The first step in deriving the 2D parallel-ray

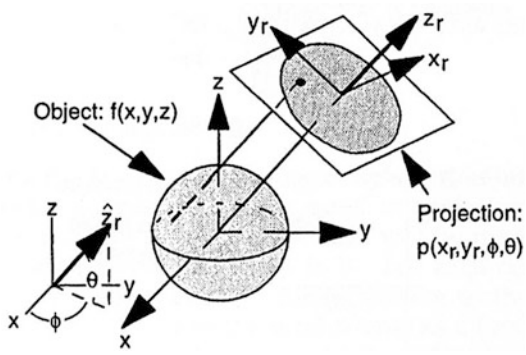

Fig. 15 In 3D PET, the projections are two-dimensional (x_r, y_r) parallel line integrals with azimuthal angle ϕ and oblique angle θ. The 3D projection data are represented as a set of sinograms, with one sinogram per polar angle θ, each row representing the projected intensity across a single polar angle θ and each column the projected intensity at the same position x_r across the projection at successive azimuthal angles ϕ (From reference [30] with permission)

projection-image data is to re-bin the 3D PET data set into a 2D data set such that each oblique (or indirect) projection ray is placed within the data for a particular non-oblique (or direct) transverse slice. The simplest approach to 3D-to-2D re-binning is known as "single-slice re-binning (SSRB)," wherein an oblique projection ray between a detector at axial position a and a detector at axial position b is positioned as if it were a projection from a directly opposed detector pair midway between these detectors (i.e., at axial position $(a + b)/2$) (Fig. 16a) [29, 31]. For projection rays at a large angle with respect to the transverse planes (i.e., corresponding to LORs between detectors located at opposite ends of the gantry), significant repositioning errors and degraded tomographic image quality result. SSRB has been replaced, therefore, with a more sophisticated and more accurate repositioning technique known as Fourier re-binning [32, 33] (Fig. 16b). In contrast to SSRB, however, Fourier re-binning cannot be performed in real-time and thus requires the full 3D data set.

Once the 3D data have thus been re-binned into 2D data, the resulting 2D fanbeam data must then be reformatted into parallel-beam data for the actual image reconstruction. The procedure for creating parallel-beam projections from fanbeam projections is shown in Fig. 17a. The resulting parallel-ray spacing Δx_r is given by:

$$\Delta x_r = \Delta d_t \sqrt{1 - \left(\frac{X_r}{R_D}\right)^2} \tag{8}$$

where $\Delta d_t = \frac{2\pi R_D}{N_D}$ is the center-to-center detector spacing of the detector elements in the transverse plane, R_D is the radius of the transaxial detector ring, and N_D is the number of detector elements in a single transaxial detector ring (Fig. 17b). Thus, as a result of the curvature of the PET gantry, the parallel-ray spacing decreases with increasing distance from the center of the detector ring. Near the center of the detector ring (i.e., for $x_r << R_D$), Δx_r can be equated with Δd_t; toward the periphery of the detector ring, however, interpolation must be performed to yield uniform parallel-ray spacing across detector gantry. This is known as the "arc correction."

The foregoing 2D parallel-beam data derived from the PET emission data (i.e., the 3D fanbeam data) can then be reconstructed into the tomographic images. There are two basic classes of image-reconstruction methods, analytic and iterative. Historically, perhaps the most widely used analytic algorithm for reconstruction of tomographic images from 2D data (or 3D data re-binned into 2D projections) has been filtered back projection (FBP) [21, 30]. In PET, however, FBP has been replaced by iterative reconstruction methods. FBP is still used rather widely in single-photon emission computed tomography (SPECT) and is discussed in ▶ Chap. 11, "Instrumentation for Single-Photon Emission Imaging". Iterative algorithms [33] attempt to progressively refine estimates of the activity distribution, rather than directly calculating the distribution, by maximizing or minimizing some "target function." The solution is said to "converge" when the difference of the target function between successive estimates (iterations) of the activity distribution is less than some prespecified value. Importantly, iterative reconstruction algorithms allow incorporation of realistic modeling of the data acquisition process (including effects of attenuation and of scatter), modeling of statistical noise,

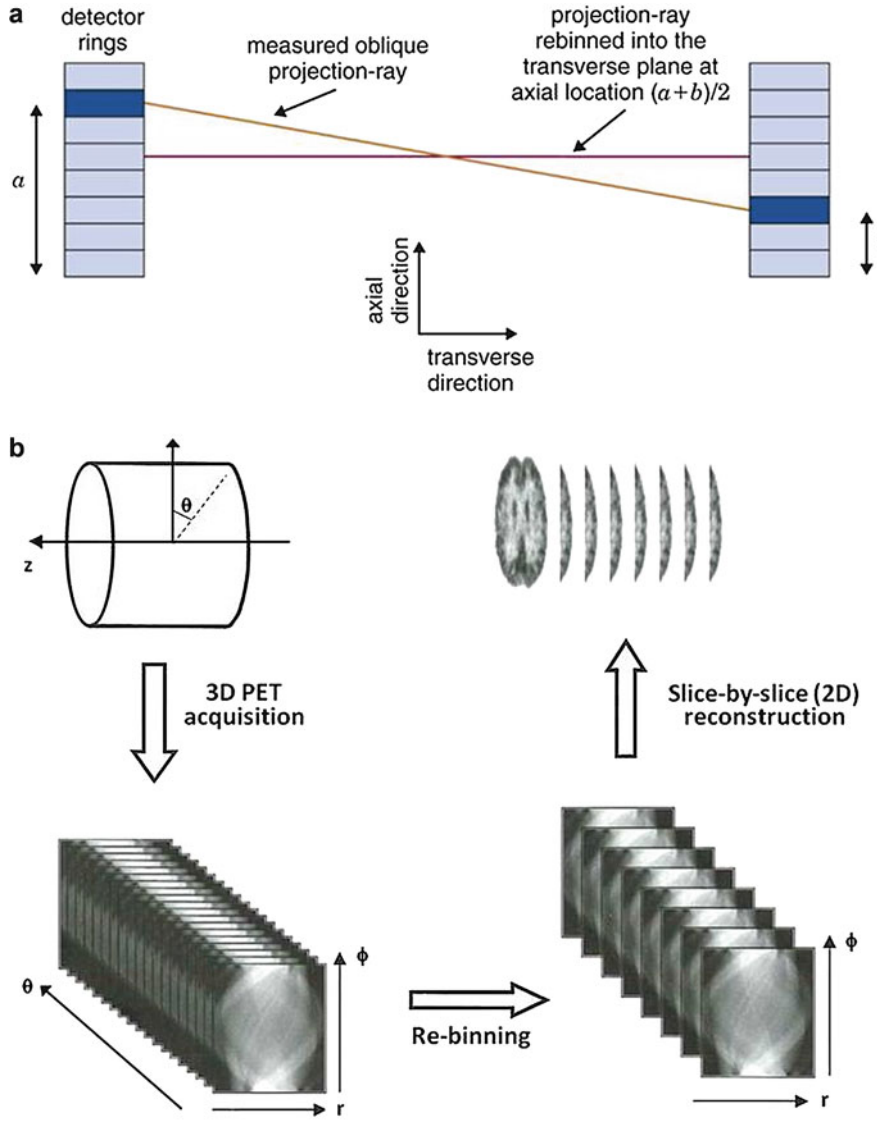

Fig. 16 **a** The single-slice re-binning algorithm in which an oblique (i.e., indirect) projection ray between detector pairs a and b is placed within the projection data for a non-oblique (i.e., direct) slice corresponding to a traverse detector pair at axial location $(a + b)/2$ (from reference [29] with permission). **b** The Fourier re-binning algorithm for re-binning 3D PET data into 2D data. The basic steps of Fourier re-binning are creating a stack of oblique sinograms, calculating the 2D Fourier transform for each oblique sinogram, normalizing the resulting 2D sinogram for the number of oblique slices contributing to the oblique sinogram, and calculating the 2D inverse Fourier transform of the resulting normalized sinograms to yield the 2D re-binned data for image reconstruction (From reference [33] with permission)

and inclusion of pertinent a priori information (e.g., only nonnegative count values). The maximum-likelihood expectation maximization (MLEM) algorithm is based on maximizing the logarithm of a Poisson-likelihood target function [34, 35]. The MLEM algorithm suppresses statistical noise, but large numbers of iterations typically are required for convergence, and therefore processing times are long. To accelerate this slow convergence, the ordered-subset expectation maximization (OSEM)

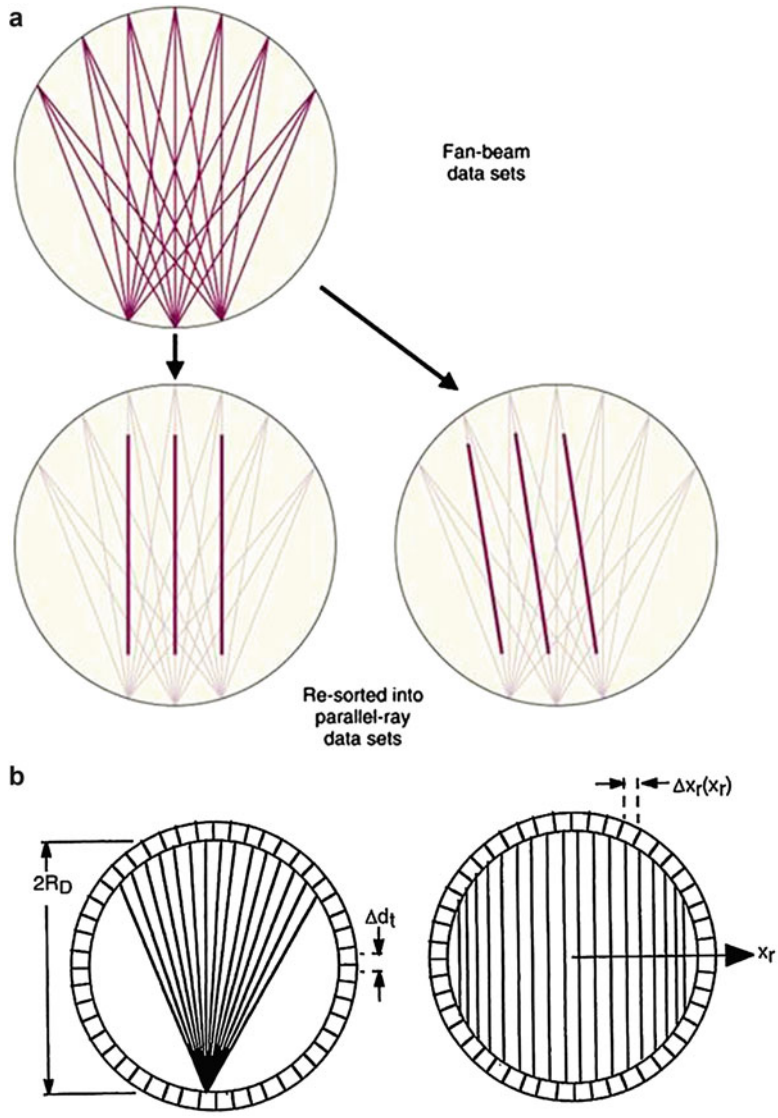

Fig. 17 **a** Procedure for creating parallel-beam projections from fanbeam projections (from reference [29] with permission). **b** Nonuniform parallel-ray spacing when creating parallel-beam projections from fanbeam projections, necessitating the so-called arc correction. (From reference [30] with permission)

algorithm [36] groups the projection data into subsets comprised of projections uniformly distributed around the source volume. The OSEM algorithm, which is a modified version of the MLEM algorithm in that the target is still maximization of the log-likelihood function, converges more rapidly than MLEM and is now the most widely used iterative reconstruction method in PET as well as SPECT [37].

In practice, OSEM is usually stopped after a relatively small number of iterations and post-filtered to dampen image noise and therefore may not achieve optimal quantitation accuracy. As an alternative to OSEM, Ahn et al., among others, have recently implemented a penalized likelihood (PL) image reconstruction algorithm in order to improve quantitation accuracy without compromising visual image quality [38]. Preliminary studies have demonstrated visual image quality including lesion conspicuity in images reconstructed by the PL algorithm is better than or at least as good as that in OSEM-reconstructed images. Despite the benefits, PL methods have not yet been widely adopted in clinical PET. Besides

computational time and complexity, the limited use of such methods in clinical PET may be that it has not been convincingly demonstrated that PL methods can provide improved quantitation accuracy compared to OSEM while maintaining clinically acceptable visual image quality.

The row-action maximization-likelihood algorithm (RAMLA), related to the OSEM algorithm, has been implemented for direct reconstruction of 3D PET data. The so-called 3D-RAMLA, which eliminates 2D re-binning of the 3D data, employs partially overlapping, spherically symmetric volume elements called "blobs" in place of voxels [37, 39, 40]. Reconstruction times are fairly long by clinical standards but the results have been excellent [41].

An important, recently introduced feature of iterative reconstruction is the 3D modeling of the scanner-specific point-spread function (PSF) map. Scanner spatial resolution deteriorates toward the periphery of the FOV but can be modeled in image reconstruction to not only improve the uniformity of spatial resolution across the FOV but also to improve spatial resolution overall. This correction is known as "resolution recovery" and is now available on most modern PET scanners. Effective tomographic image resolution as low as 2 mm has been achieved using resolution recovery.

Quantitation

Once the emission data have been corrected for dead time, randoms, system response (by normalization), scatter, and attenuation, the count rate per voxel in the reconstructed tomographic images is proportional to the local activity concentration. A factor which adversely effects the quantitative accuracy of PET is partial-volume averaging: for a source which is "small" relative to the spatial resolution of the imaging system, the image-derived activity or activity concentration in such a source underestimates the actual value, and the smaller the source, the greater the degree of the underestimation [24, 42]. The dimensions of a source must be at least two times the FWHM spatial resolution of the imaging system to avoid such underestimation of the activity or activity concentration [42]. Since the source-size dependence of the partial-volume effect can be measured (e.g., by phantom studies), the underestimated activity or activity concentration can be corrected if the source dimensions can be independently determined (e.g., by CT) [43]. Another key factor which limits the quantitative accuracy of SPECT and PET is subject motion. As in photography, subject motion blurs PET images, dispersing the counts in a source region over an apparently larger volume than the actual volume of that region. This results not only in an overestimate of the source region volume but also an underestimate of the source region activity concentration. For sources (e.g., tumors) in the lung and the dome of the liver, a particularly important source of such inaccuracies is respiratory motion [44–47]. Practical, reasonably accurate methods for respiratory gating of PET studies have been developed and result in more reliable estimates of the volumes and activity concentrations in pulmonary lesions [44–47].

To make the images absolutely quantitative, the count rate per voxel (cps), $\dot{C}_{ijk}$, in voxel *ijk* must be divided by a measured system calibration factor ((μCi/cc)/(cps/voxel)), CF, to yield the activity concentration [7]:

$$\{A\}_{ijk} = \frac{\dot{C}_{ijk}}{CF} \tag{9}$$

where $\{A\}_{ijk}$ is the activity concentration (e.g., μCi/cc) in voxel *ijk*. The calibration factor (CF) can be derived by scanning a calibrated standard, that is, a water-filled or water (tissue)-equivalent volume source with all linear dimensions at least twice that of the system spatial resolution and with a uniform, well-defined activity concentration at the time of the scan. The requirement for water equivalence is to ensure that effects such as scatter and attenuation are comparable in both the subject and the standard. And the requirement for linear dimensions at least twice that of the system spatial resolution is to ensure that the effect of partial-volume averaging and associated underestimation of local count rates is negligible. Activity concentration

is often expressed in terms of the decay-corrected fraction or percent of the administered activity per cubic centimeter (cc) or, more commonly in clinical PET, in terms of the standard uptake value (*SUV*):

$$SUV = \frac{\mu\text{Ci/cc of tissue}}{\mu\text{Ci injected/gm body mass}} \qquad (10)$$

An advantage of using *SUV* to express activity concentration is that, in first order, it is independent of the body mass of the subject.

The practical quantitative accuracy of PET (expressed, e.g., as the percent difference between the image-derived and actual activity or activity concentration in a source region) is difficult to characterize unambiguously, as it depends on such factors as the count statistics, the size of the source region, the source-to-background activity concentration ratio, the subject motion, and the accuracy of all applicable corrections. Under favorable circumstances (i.e., for a high-count study of a large, stationery source region with a high source-to-background ratio), the accuracy of the PET is of the order of 10% [42].

Multimodality Devices

Image registration and fusion have become increasingly important components of both clinical and laboratory imaging and have led to the development of a variety of pertinent software and hardware tools, including multimodality devices which transparently provide registered and fused 3D image sets [48–52]. In addition to anatomic localization of signal foci, image registration and fusion provide intra- as well as inter-modality corroboration of diverse images and more accurate and more certain diagnostic and treatment-monitoring information. There are two practical approaches to image registration and fusion, "software" and "hardware" approaches. In the software approach, images are acquired on separate devices, imported into a common image-processing computer platform, and registered and fused using the appropriate software. In the hardware approach, images are acquired on a single, multimodality device and transparently registered and fused with the manufacturer's integrated software. Both approaches are dependent on software sufficiently robust to recognize and import diverse image formats. The availability of industry-wide standard formats, such as the ACR-NEMA DICOM standard (i.e., the American College of Radiology (ACR) and National Electrical Manufacturers Association (NEMA) for Digital Imaging and Communications in Medicine (DICOM) standard [53, 54]), is therefore critical.

PET/MRI. All manufacturers of PET and CT scanners market multimodality scanners, combining PET with CT scanners in a single device. These instruments provide near-perfect registration of images of in vivo function (PET) and anatomy (CT) using a measured, and presumably fixed, rigid transformation (i.e., translation and rotation in three dimensions) between the image sets. The rigid transformation matrix can be used to align the PET and the CT image sets. This matrix can be measured using a phantom, that is, an inanimate object with PET- and CT-visible landmarks arranged in a well-defined geometry. The transformation matrix required to align these landmarks can then be stored and used to automatically register *all* subsequent multimodality studies, since the device's geometry and therefore this matrix should be fixed. Although generally encased in a single seamless housing, the PET and CT gantries in such multimodality devices are separate; the respective fields of view are separated by a distance of the order of 1 m, and the PET and CT scans are performed sequentially.

PET/MRI. Despite its unquestioned clinical utility, PET/CT has certain notable shortcomings, including the inability to perform simultaneous data acquisition, the significant radiation dose to the patient contributed by CT, and the inability of non-contrast CT to distinguish different soft tissues [55–57]. Compared to CT, MRI provides not only better contrast among soft tissues but also functional imaging capabilities. The combination of PET/MRI may thus provide advantages which go well beyond simply combining functional

information with structural MRI information. Among multimodality imaging studies, therefore, PET/MRI may ultimately provide the greatest yield of information by combining the quantitative molecular imaging capabilities of PET (including the large number and variety of radiotracers) with the excellent anatomic resolution, marked soft tissue contrast, and functional imaging capabilities provided by MRI (e.g., perfusion by dynamic contrast-enhanced (DCE) imaging) and magnetic resonance spectroscopic imaging (MRSI) (e.g., quantitation of regional concentrations of metabolites such as lactate, citrate, and choline) [55–57].

As noted, an important advantage of PET/MRI is that the image data can be acquired *simultaneously* because the PET and MR imaging signals (i.e., gamma- or X-rays and radiofrequency (RF) waves, respectively) do not interfere with one another. Registration of sequentially acquired functional and structural images is very forgiving of the short time interval (typically only several minutes) between the PET and CT scans, as anatomy does not actually change over such short time intervals (except, perhaps, for filling of the urinary bladder, transit of gas through the bowel, etc.). Registration of sequentially acquired functional images, however, is potentially more problematic, as functional properties, such as blood flow, hypoxia, neuronal activation, etc., may change transiently over time frames of minutes and even seconds. However, many technical challenges, related to possible interference between the modalities' hardware, have to be solved when combining PET and MRI [55, 57–65]. Most notably, conventional PET and SPECT detectors are based on PMTs, which do not operate properly in the presence of a magnetic field, and various approaches have been pursued to overcome this and other challenges in combining nuclear and MR modalities. The most straightforward approach is placement of the PET and MR scanners in series in a manner analogous to current PET/CT devices. However, this would require magnetic shielding of the PET scanner and/or imposition of a relatively large distance between the PET and MR scanners. Further, because data acquisition for PET and MRI individually is time-consuming, sequential imaging may result in prohibitively long overall study times (well over 1 h) in a clinical setting. Space constraints are also a consideration. Most importantly, physical separation of the scanners would eliminate the ability to perform the nuclear and MR scans simultaneously, which, as noted, is perhaps the most compelling feature of such hybrid devices. The preferable approach, therefore, is integration of the PET hardware into the MR gantry.

Due to its various hardware components, the PET subsystem can interfere with the performance of the MRI subsystem by compromising the homogeneity of the MRI's main magnetic field and the RF field and thereby degrade MR image quality. BGO and LSO crystals, for example, produce only minor magnetic-field distortion, while GSO and LYSO have sharply different magnetic susceptibilities than tissue and thus markedly distort MR images. At the same time, the variable MR gradients may induce eddy currents in conductive materials of the nuclear detectors and distort the effective applied gradient field. As noted, the effects of the high magnetic fields of the MR subsystem exclude the use of PMTs employed in conventional PET detectors, as the path of the electrons between the dynodes in the evacuated PMT is deflected from their normal trajectory by the external magnetic field [55, 66]. In addition, the RF fields and also the gradient system pulses of the MR subsystem can degrade the performance of and even damage the PET electronics. One approach to overcoming this limitation is the use of long optical fibers (up to several meters in length) to couple the detector crystal to a PMT positioned outside the MR subsystem's fringe field (i.e., at magnetic fields of no greater than 10 mT). In this way, only the X-ray and γ-ray detection elements lie within the magnetic field, and the scintillations are directed out of the field by the fibers. Despite the challenges presented by such systems, including the large number of optical fibers required (one per detector element) and partial loss of the light signal over the length of the fibers, several prototypes of such PET/MRI scanners (with field strengths up to 3 T) have been fabricated.

An alternative, and ultimately more practical approach, to PET/MRI is elimination of the PMTs

altogether by using solid-state scintillation detectors such as APDs or SiPMs. APDs and SiPMs are relatively insensitive to magnetic fields and thus can be coupled directly to the scintillation detector blocks via conventional (i.e., short) light guides. It is still important, however, to provide RF shielding of the PET subsystem components within the magnetic field, for example, using copper mesh.

MR images do not directly provide attenuation information, and in PET/MR systems, the attenuation correction maps must therefore be estimated indirectly. Software methods have been proposed for MR-based attenuation correction, based on image segmentation or co-registration of templates with preassigned tissue-specific attenuation coefficients. A method proposed by Martinez-Moeller et al. has been utilized in clinical systems, with a two-point Dixon VIBE MR sequence to obtain fat and water compartments for calculating attenuation. Lung tissue in the MR images is identified by image segmentation. Software-constructed attenuation maps obtained from MR may not reflect true photon attenuation, since several classes of tissue can be defined. In addition, the actual attenuation coefficients may be different than standard assumed values.

Commercial Devices

Clinical. All of the major manufacturers of medical imaging equipment, including General Electric, Philips, Siemens, and Toshiba, currently market clinical PET devices (Tables 4 and 5, respectively). Since 2005, PET scanners have been marketed exclusively as multimodality (i.e., PET/CT) scanners; clinical "PET-only" scanners are no longer marketed. The PET subsystems of commercial PET/CT scanners utilize BGO, LSO, or LYSO as the detector material, with most now operating exclusively in 3D mode and all except the BGO-based systems incorporating TOF capability. The dimensions of the detector elements are typically $4 \times 4 \times 20$ mm^3, though slightly larger-area and thicker detector elements are found in some units. The axial fields of view are typically 20 cm in length, and whole-body studies therefore require six or seven bed positions. PET system spatial resolution (FWHM) is of the order 5 mm among clinical systems. The design and performance parameters of the PET subsystem of currently marketed clinical whole-body PET/CT scanners are summarized in Table 3 [5].

Several "special-purpose" clinical scanners have been marketed as well. These include positron emission mammographs (PEMs) [67]. The PEM Flex Solo II (Naviscan PET Systems, Inc.) [68] is a limited-angle, focal-plane tomography system with two opposed 6×16.4-cm^2 LYSO detectors ($2 \times 2 \times 13$-mm^3 detector elements) backed by PSPMTs and mounted inside compression paddles for immobilization and compression of the breast. The detectors, mounted on an articulating arm that rotates to allow imaging from different views, can scan up to 24 cm across the FOV in the direction of their 6-cm dimension, yielding a maximum FOV of 24×16.4 cm^2. The PEM Flex Solo II, with an in-plane spatial resolution of ~2.5 mm, thus differs markedly from conventional PET scanners in that the detectors do not encircle the object (in this case, the breast) being imaged.

At least two PET/MRI systems capable of simultaneously collecting MR and PET image data with almost no degradation of either MR or PET performance are now commercially available from Siemens and General Electric [5]. As previously discussed, simultaneous acquisition of MR and PET data presents significant engineering challenges due to cross interference between PET and MR hardware. To minimize this cross interference in the PET subsystem, PMTs are replaced with APDs and SiPMs in the Siemens and General Electric systems, respectively. The Siemens mMR™ system is based on a Verio™ MR scanner with a modified body radiofrequency (RF) coil, gradient coil, and patient-handling system. In this system, the APD PET detectors are arrayed around a cylinder that is inserted into the bore of the MR scanner, reducing the bore diameter from 70 to 60 cm. LSO scintillator crystals ($4 \times 4 \times 20$ mm^3) are arranged in eight rings of 56 blocks comprised of 8×8 crystals backed by a 3×3 array of APDs per block. The MR

Table 3 Design and performance parameters of the PET subsystem in current commercially available clinical PET/CT scanners [5]

PET/CT model	Ingenuity TF	Discovery 710	Biograph mCT flow (TrueV)	Discovery IQ (5 rings)	Vereos
Patient port (cm)	70 Open view	70	78	70	70
CT (slices)	64, 128	16, 64, 128	20, 40, 64	16	64, 128
Patient scan range (cm)	190	200	195	200	190
Maximum patient weight (kg [lb])	195 (430)	226 (500)	226 (500)	226 (500)	195 (430)
Acquisition modes	3D S&S	3D S&S	3D S&S and continuous	3D S&S	3D S&S
Number of image planes	45 or 90	47	109	79	72
Plane spacing (mm)	2 or 4	3.27	2	3.27	1, 2, or 4
Crystal size (mm^3)	4 × 4 × 22	4.2 × 6.3 × 25	4 × 4 × 20	6.3 × 6.3 × 30	4 × 4 × 22
Number of crystals	28,336	13,824	32,448	19,200	23,040
Number of PMTs	420	256	768	720	SiPM
Physical axial FOV (cm)	18	15.7	21.8	26	16.3
Detector material	LYSO	LYSO	LSO	BGO	LYSO
System sensitivity (%)	0.74	0.75	0.95	2.2	2.2[b]
Transaxial resolution at 1 cm (mm)[a]	4.7	4.9	4.4	4.9	4.0
Transaxial resolution at 10 cm (mm)[a]	5.2	5.5	4.9	5.5	4.5
Axial resolution at 1 cm (mm)[a]	4.7	5.6	4.5	5.1	4.0
Axial resolution at 10 cm (mm)[a]	5.2	6.3	5.9	5.5	4.5
Peak NECR (kcps) at kBq/ml[a]	120 at 19 kBq/ml	130 at 29.5 kBq/ml	175 at 28 kBq/ml	120 at 9 KBq/ml	650 at 50 kBq/ml
Time-of-flight resolution (picoseconds)	550	544	540	n.a.	345
Time-of-flight localization (cm)	8.9	8.2	8.1	n.a.	5.2
Coincidence window (nanoseconds)	4.5	4.9	4.1	9.5	1.5

S&S Step-and-shoot whole-body scanning, *n.a.* Not applicable

[a] Performance measurements of positron emission tomographs. NEMA Standards Publication NU 2-2001 [72]

[b] Vendor-defined "effective sensitivity," which includes TOF positioning gain

Table 4 Design and performance parameters of current commercially available clinical PET-MR scanners [5]

PET/MR model	GE Signa	mMR
Patient port (cm)	60	60
MR model (3 T)	Discovery 750 w (3 T)	Verio
Patient scan range (cm)	188 (PET)/205 (MR)	200
Maximum patient weight (kg [lb])	226 (500)	200 (441)
Acquisition modes	3D and S&S	3D S&S
Number of image planes	89	127
Plane spacing (mm)	2.8	2
Crystal size (mm^3)	4 × 5.3 × 25	4 × 4 × 20
Number of crystals	20,160	28,672
Number of PMTs	SiPM	APD
Physical axial FOV (cm)	25	25.8
Detector material	LYSO	LSO
System sensitivity at 0 cm (%)[a]	2.1	1.5
Transaxial resolution at 1 cm (mm)[a]	4.2	4.1
Transaxial resolution at 10 cm (mm)[a]	5.2	5.2
Axial resolution at 1 cm (mm)[a]	5.8	4.3
Axial resolution at 10 cm (mm)[a]	7.1	6.6
Peak NECR (kcps)[a]	210 at 17.5 kBq/ml	175 at 21.8 kBq/ml
Time-of-flight resolution (picoseconds)	400	n.a.
Time-of-flight localization (cm)	6.0	n.a.
Coincidence window (nanoseconds)	4.6	5.9

S&S Step-and-shoot whole-body scanning, *n.a.* Not applicable

[a] Performance measurements of positron emission tomographs. NEMA Standards Publication NU 2-2001 [72]

gradient system is cooled and the PET detectors are shielded with copper to reduce electromagnetic interference. The APDs do not distort the main magnetic field, and the acquisitions of the MR and PET subsystems are synchronized to reduce possible distortion of the PET signals by the MR RF and gradient pulses. The PET component of the Siemens scanner has a 25.8-cm axial FOV. However, this system does not offer TOF capability, due to relatively low timing resolution of APDs. The GE Signa™ PET-MR uses SiPMs to achieve TOF with a coincidence timing resolution of 400 and 390 ps with RF "on" and "off," respectively. It offers a 25-cm PET axial FOV and a sensitivity of 2.1%. The PET subsystem comprises five rings of 112 detector blocks (each a 4 × 9 array of LYSO crystals, 3.95 × 5.3 × 25 mm^3) backed by a 1 × 3 arrays of SiPMs. The PET detector ring is centered inside the MR gradient set of a GEMR750w™ 3 T scanner on the outer diameter of the RF body coil. Figure 18 shows the digital PET detector modules used in the Siemens mMR™ and the GE Signa™ PET/MR systems [5] and Table 4 [5] the design and performance parameters of these systems.

Preclinical. A number of preclinical PET devices are commercially available, both from major manufacturers and smaller "niche" companies. Preclinical PET scanners, which operate exclusively in 3D mode, are diverse in design, utilizing different scintillation detectors in combination with either PSPMTs or APDs. The superior spatial resolution of preclinical versus clinical PET scanners, 1–2 mm versus 4–6 mm, is due in part to the much smaller gantry diameter and therefore a less pronounced resolution-degrading effect of the non-colinearity of the annihilation γ-rays. Preclinical devices are currently marketed as "PET-only" scanners or as multimodality devices with integrated CT scanners, typically conebeam devices with flat-panel detectors. The Carestream Albira™, Gamma Medica Triumph LabPET Solo™, and Siemens Inveon™ are available as trimodality PET-SPECT/CT systems. The design and performance parameters of currently marketed preclinical PET scanners are summarized in Table 5.

Table 5 Design and performance parameters of current commercially preclinical PET scanners

	Bioscan (Philips) NanoPET	Bioscan BioPET	Carestream Albira	Clairvivo PET	Gamma Medica Triumph LabPET Solo	Oxford quad HIDAC	Ray test ClearPET	Sedecal Argus[a]	Siemens Inveon	Genisys Sofie
Detectors	LYSO + PSPMTs[b]	Phoswich (LYSO + GSO) + APDs[c]	LYSO + PSPMTs[a]	LYSO + PSPMTs[a]	Phoswich (LYSO + GSO) + APDs	Multi-wire proportional gas chambers	Phoswich (LYSO + LuYAP) + PSPMTs	Phoswich (LYSO + GSO)	LSO + PSPMTs[a]	BGO
Transaxial FOV[d] (cm)	Up to 12.5		8.0	10.2	3.7	0	14 – Mice[e] 27 – Rats[e]	6.8	10.0	4.4
Axial FOV[d](cm)	3.0		Up to 14.8	15.1	Up to 10	28	Not available	4.7	12.7	9.5
Detector elements (mm^3)	1.12 × 1.12 × 13	1.45 × 1.45 × 15	n.a.	1.28 × 2.68 × 7	n.a.	n.a.	2.0 × 2.0 × 10	1.45 × 1.45 × 15	1.59 × 1.59 × 10	1.8 × 1.2 × 7
Spatial resolution (FWHM in mm)	1.2		1.4	1.5	1.0–1.4	0.9	1.4	1.1	1.4	1.4
Sensitivity (%)	8.3		Up to 9	8.2	Not available	1.8	Not available	6.5	10	14

Preclinical scanners are all operate exclusively in 3D mode and are currently marketed as "PET-only" scanners or as multimodality devices with integrated CT and/or SPECT scanners. The Carestream Albira, Gamma Medica Triumph LabPET Solo, and Siemens Inveon are available as trimodality PET-SPECT/CT systems

Extracted from the marketing literature of the respective manufacturers and from references [12, 73–75]

[a]Formerly the General Electric eXplore Vista

[b]PSPMTs: Position-sensitive photomultiplier tubes

[c]APDs: Avalanche photodiodes

[d]FOV: Field of view

[e]The Ray Test ClearPET has an adjustable detector ring diameter, and the detector rings rotate at the larger diameter to compensate for the space between detector blocks at the larger diameter

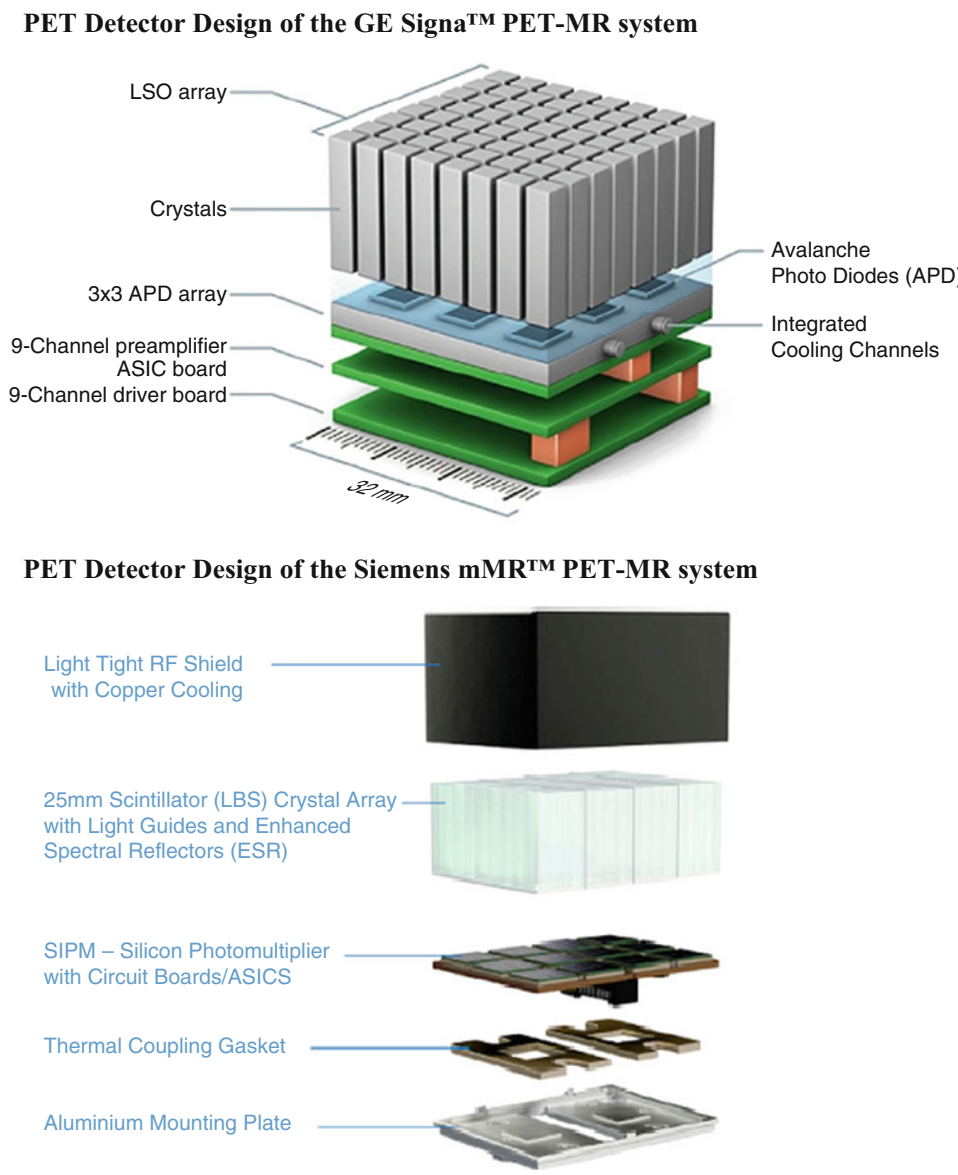

Fig. 18 The digital PET detector modules used in the Siemens mMR™ and the GE Signa™ PET/MR systems (From reference [5] with permission)

Concluding Remarks

The use of PET and of PET/CT has grown dramatically over the last several decades. In contrast to PET/CT, however, where there are temporal and spatial offsets between the PET and the CT studies, PET and MRI studies (including dynamic studies) can be performed simultaneously. The recent introduction of PET/MRI [55–57, 64] multimodality devices will no doubt lead to new and important applications of molecular imaging [69].

References

1. Zanzonico P. Principles of nuclear medicine imaging: planar, SPECT, PET, multi-modality, and autoradiography systems. Radiat Res. 2012;177:349–64.
2. Zanzonico P, Heller S. Physics, instrumentation, and radiation protection. In: Biersack HJ, Freeman LM, editors. Clinical nuclear medicine. Heidelberg: Springer; 2007. p. 1–33.
3. Zanzonico P. Radionuclide imaging. In: Cherry S, Badawy R, Qi J, editors. Essentials of in vivo biomedical imaging. Boca Raton: CRC Press; 2015. p. 1765–224.
4. Otte N. The silicon photomultiplier – a new device for high energy physics, astroparticle physics, industrial and medical applications, in SNIC symposium. Palo Alto: STanford University; 2006.
5. Slomka PJ, Pan T, Germano G. Recent advances and future progress in PET instrumentation. Semin Nucl Med. 2016;46:5–19.
6. Humm JL, Rosenfeld A, Del Guerra A. From PET detectors to PET scanners. Eur J Nucl Med Mol Imaging. 2003;30:1574–97.
7. Zanzonico P. Positron emission tomography: a review of basic principles, scanner design and performance, and current systems. Semin Nucl Med. 2004;34:87–111.
8. Zanzonico P, Heller S. The intraoperative gamma probe: basic principles and choices available. Semin Nucl Med. 2000;30:33–48.
9. Heller S, Zanzonico P. Nuclear probes and intraoperative gamma cameras. Semin Nucl Med. 2011;41:166–81.
10. Townsend DW, Bendriem B. Introduction to 3D PET. In: Bendriem B, Townsend DW, editors. The theory and practice of 3D PET. Dordrecht: Kluwer Academic Publishers; 1998. p. 1–10.
11. Cherry SR, Sorenson JA, Phelps ME. Physics in nuclear medicine. 3rd ed. Philadelphia: Saunders; 2003.
12. Mosset JB, Devroede O, Krieguer M, et al. Development of an optimised LSO/LuYAP phoswich detector head for the ClearPET camera. In: Nuclear science symposium conference record, 2004 IEEE. Lyon: Institute of Electrical and Electronics Engineers; 2004. p. 2439–2443.
13. Lewellen TK. Time-of-flight PET. Semin Nucl Med. 1998;28:268–75.
14. Moses WW. Recent advances and future advances in time-of-flight PET. Nucl Instrum Methods Phys Res A. 2007;580:919–24.
15. Karp JS, Surti S, Daube-Witherspoon ME, et al. Benefit of time-of-flight in PET: experimental and clinical results. J Nucl Med. 2008;49:462–70.
16. Levin CS, Hoffman EJ. Calculation of positron range and its effect on the fundamental limit of positron emission tomography system spatial resolution. Phys Med Biol. 1999;44:781–99.
17. Derenzo SE. Mathematical removal of positron range blurring in high-resolution tomography. IEEE Trans Nucl Sci. 1986;NS-33:565–9.
18. Berko S, Hereford FL. Experimental studies of positron interactions in solids and liquids. Rev Modern Phys. 1956;28:299–307.
19. Yang Y, Wu Y, Qi J, et al. A prototype PET scanner with DOI-encoding detectors. J Nucl Med. 2008;49:1132–40.
20. Zanzonico P. Routine quality control of clinical nuclear medicine instrumentation: a brief review. J Nucl Med. 2008;49:1114–31.
21. Zanzonico PB. Technical requirements for SPECT: equipment and quality control. In: Kramer EL, Sanger JJ, editors. Clinical applications in SPECT. New York: Raven; 1995. p. 7–41.
22. Hoffman EJ, Huang SC, Phelps ME, et al. Quantitation in positron emission computed tomography: 4. Effect of accidental coincidences. J Comput Assist Tomogr. 1981;5:391–400.
23. Rokitta O, Casey M, Wienhard K, Pictrzyk U. Random correction for positron emission tomography using singles count rates. In: Merelli D, Surget J, Ulma M, editors. Nuclear science symposium conference record, 2000 IEEE. Lyon: Institute of Electrical and Electronics Engineers; 2000. p. 1737–1740.
24. Frey EC, Humm JL, Ljungberg M. Accuracy and precision of radioactivity quantification in nuclear medicine images. Semin Nucl Med. 2012;42:208–18.
25. Meikle SR, Badawi RD, et al. Quantitative techniques in PET. In: Bailey DL, editor. Positron emission tomography: basic sciences. London: Springer; 2005. p. 93–126.
26. Bailey DL. Quantitative procedures in 3D PET. In: Bendriem B, Townsend DW, editors. The theory and practice of 3D PET. Dordrecht: Kluwer Academic Publishers; 1998. p. 55–109.
27. Cherry SR, Huang SC. Effects of scatter on model parameter estimates in 3D PET studies of the human brain. IEEE Trans Nucl Sci. 1995;42:1174–9.
28. Stearns CW. Scatter correction method for 3D PET using 2D fitted Gaussian functions. J Nucl Med. 1995;36:105P.
29. Cherry SR, Sorenson JA, Phelps ME. Physics in nuclear medicine. 4th ed. Philadelphia: Saunders; 2012.
30. Defrise M, Kinahan P. Data acquisition and image reconstruction for 3D PET. In: Bendriem B, Townsend DW, editors. The theory and practice of 3D PET. Dordrecht: Kluwer Academic Publishers; 1998. p. 11–53.
31. Daube-Witherspoon ME, Muehllehner G. Treatment of axial data in three-dimensional PET. J Nucl Med. 1987;28:1717–24.
32. Defrise M, Kinahan PE, Townsend DW, et al. Exact and approximate rebinning algorithms for 3-D PET data. IEEE Trans Med Imaging. 1997;16:145–58.
33. Defrise MK, Kinahan PE, Michel CJ. Image reconstruction algorithms in PET. In: Bailey DL, Townsend DW, Valk PE, Maisey MN, editors. Positron emission tomography: basic sciences. London: Springer; 2005. p. 63–91.

34. Miller TR, Wallis JW. Fast maximum-likelihood reconstruction. J Nucl Med. 1992;33:1710–1.
35. Miller TR, Wallis JW. Clinically important characteristics of maximum-likelihood reconstruction. J Nucl Med. 1992;33:1678–84.
36. Hudson HM, Larkin RS. Accelerated image reconstruction using ordered subsets of projection data. IEEE Trans Med Imaging. 1994;13:601–9.
37. Tarantola G, Zito F, Gerundini P. PET instrumentation and reconstruction algorithms in whole-body applications. J Nucl Med. 2003;44:756–69.
38. Ahn S, Ross SG, Asma E, et al. Quantitative comparison of OSEM and penalized likelihood image reconstruction using relative difference penalties for clinical PET. Phys Med Biol. 2015;60:5733–51.
39. Matej S, Lewitt RM. Efficient 3D grids for image reconstruction using spherical-symmetric volume elements. IEEE Trans Nucl Sci. 1996;42:1361–70.
40. Matej S, Lewitt RM. Practical considerations for 3-D image reconstruction using spherically symmetric volume elements. IEEE Trans Med Imaging. 1996;15: 68–78.
41. Daube-Witherspoon ME, Matej S, Karp JS, et al. Application of the 3D row action maximum likelihood algorithm to clinical PET imaging. IEEE Trans Nucl Sci. 2001;48:24–30.
42. Hoffman EJ, Huang SC, Phelps ME. Quantitation in positron emission computed tomography: 1. Effect of object size. J Comput Assist Tomogr. 1979;3:299–308.
43. Erlandsson K, Buvat I, Pretorius PH, Thomas BA, Hutton BF. A review of partial volume correction techniques for emission tomography and their applications in neurology, cardiology and oncology. Phys Med Biol. 2012;57:R119–59.
44. Nehmeh SA, Erdi YE. Respiratory motion in positron emission tomography/computed tomography: a review. Semin Nucl Med. 2008;38:167–76.
45. Nehmeh SA, Erdi YE, Ling CC, et al. Effect of respiratory gating on quantifying PET images of lung cancer. J Nucl Med. 2002;43:876–81.
46. Nehmeh SA, Erdi YE, Ling CC, et al. Effect of respiratory gating on reducing lung motion artifacts in PET imaging of lung cancer. Med Phys. 2002; 29:366–71.
47. Nehmeh SA, Erdi YE, Rosenzweig KE, et al. Reduction of respiratory motion artifacts in PET imaging of lung cancer by respiratory correlated dynamic PET: methodology and comparison with respiratory gated PET. J Nucl Med. 2003;44:1644–8.
48. Israel O, Goldsmith SJ, editors. Hybrid SPECT/CT: imaging in clinical practice. New York: Taylor & Francis; 2006. p. 244.
49. Townsend DW. A combined PET/CT scanner: the choices. J Nucl Med. 2001;42:533–4.
50. Townsend DW, Beyer T. A combined PET/CT scanner: the path to true image fusion. Br J Radiol. 2002;75 (Spec No):S24–30.
51. Townsend DW, Beyer T, Blodgett TM. PET/CT scanners: a hardware approach to image fusion. Semin Nucl Med. 2003;33:193–204.
52. Townsend DW. Positron emission tomography/computed tomography. Semin Nucl Med. 2008;38:152–66.
53. Horii S. ACR-NEMA DICOM support for exchange media: a report on the activity of working group V. Adm Radiol. 1993;12:68–9.
54. Bidgood Jr WD, Horii SC. Introduction to the ACR-NEMA DICOM standard. Radiographics. 1992; 12:345–55.
55. Pichler BJ, Kolb A, Nagele T, et al. PET/MRI: paving the way for the next generation of clinical multimodality imaging applications. J Nucl Med. 2010;51:333–6.
56. Pichler BJ, Wehrl HF, Kolb A, et al. Positron emission tomography/magnetic resonance imaging: the next generation of multimodality imaging? Semin Nucl Med. 2008;38:199–208.
57. Judenhofer MS, Wehrl HF, Newport DF, et al. Simultaneous PET-MRI: a new approach for functional and morphological imaging. Nat Med. 2008; 14:459–65.
58. Judenhofer MS, Cherry SR. Applications for preclinical PET/MRI. Semin Nucl Med. 2013;43:19–29.
59. Ng TS, Bading JR, Park R, et al. Quantitative, simultaneous PET/MRI for intratumoral imaging with an MRI-compatible PET scanner. J Nucl Med. 2012;53: 1102–9.
60. Peng BJ, Walton JH, Cherry SR, et al. Studies of the interactions of an MRI system with the shielding in a combined PET/MRI scanner. Phys Med Biol. 2010; 55:265–80.
61. Pichler BJ, Judenhofer MS, Catana C, et al. Performance test of an LSO-APD detector in a 7-T MRI scanner for simultaneous PET/MRI. J Nucl Med. 2006;47:639–47.
62. Hofmann M, Pichler B, Scholkopf B, et al. Towards quantitative PET/MRI: a review of MR-based attenuation correction techniques. Eur J Nucl Med Mol Imaging. 2009;36 Suppl 1:S93–104.
63. Kolb A, Wehrl HF, Hofmann M, et al. Technical performance evaluation of a human brain PET/MRI system. Eur Radiol. 2012;22:1776–88.
64. Pichler BJ, Judenhofer MS, Wehrl HF. PET/MRI hybrid imaging: devices and initial results. Eur Radiol. 2008;18:1077–86.
65. Sauter AW, Wehrl HF, Kolb A, et al. Combined PET/MRI: one step further in multimodality imaging. Trends Mol Med. 2010;16:508–15.
66. Catana C, Wu Y, Judenhofer MS, et al. Simultaneous acquisition of multislice PET and MR images: initial results with a MR-compatible PET scanner. J Nucl Med. 2006;47:1968–76.
67. Moadel RM. Breast cancer imaging devices. Semin Nucl Med. 2011;41:229–41.
68. MacDonald L, Edwards J, Lewellen T, et al. Clinical imaging characteristics of the positron emission

mammography camera: PEM Flex Solo II. J Nucl Med. 2009;50:1666–75.
69. Beyer T, Freudenberg LS, Czernin J, et al. The future of hybrid imaging-part 3: PET/MR, small-animal imaging and beyond. Insights Imaging. 2011;2:235–46.
70. Firestone RB, Shirley VS, editors. Table of isotopes. 8th ed. New York: Wiley; 1996.
71. Weber D, Eckerman K, Dillman L, et al., editors. MIRD: radionuclide data and decay schemes. New York: Society of Nuclear Medicine; 1989. p. 447.
72. NEMA. Performance measurements of positron emission tomographs. NEMA Standards Publication NU 2-2001. Rosslyn: National Electrical Manufacturers Association (NEMA); 2001.
73. Larobina M, Brunetti A, Salvatore M. Small animal PET: a review of commercially available imaging systems. Curr Med Imaging Rev. 2006;2:187–92.
74. Constantinescu CC, Mukherjee J. Performance evaluation of an Inveon PET preclinical scanner. Phys Med Biol. 2009;54:2885–99.
75. Mizuta T, Kitamura K, Iwata H, et al. Performance evaluation of a high-sensitivity large-aperture small-animal PET scanner: clear PET. Ann Nucl Med. 2008; 22:447–55.